State of Charge Estimation for Rechargeable Batteries Based on the Nonlinear Double-Capacitor Model

Mason J. Proctor

B.S. Mechanical Engineering, University of Kansas, 2017

Submitted to the graduate degree program in Department of Mechanical Engineering and the Graduate Faculty of the University of Kansas in partial fulfillment of the requirements for the degree of Master of Science.

Committee members

Huazhen Fang, Chairperson

Xianglin Li, Chair Member

Sara Wilson, Chair Member

Date defended: May 13, 2021

The Thesis Committee for Mason J. Proctor certifies
that this is the approved version of the following thesis :

State of Charge Estimation for Rechargeable Batteries Based on the Nonlinear Double-Capacitor
Model

_____

Huazhen Fang, Chairperson

Date approved: _____ June___ , 2021 _____

Abstract

State of charge (SOC) estimation plays a foundational role in advanced battery management systems, having attracted much attention in the past decade. It is widely acknowledged that the accuracy of SOC estimation largely depends on the accuracy of the selected model. In this thesis, SOC estimation methods are developed based on the nonlinear double-capacitor (NDC) model, a novel equivalent circuit model that is distinctly capable of simulating the charge diffusion inside an electrode of a battery and capturing the battery's nonlinear voltage behavior simultaneously. With improved predictive accuracy, the NDC model provides a new opportunity for enabling more accurate SOC estimation. With this motivation, the well-known extended Kalman filter (EKF) and unscented Kalman filter (UKF) are utilized to perform SOC estimation based on the NDC model. The EKF is desirable here as it leads to efficient computation, straightforward implementation, and good convergence in its application to the NDC model, which is low-dimensional and governed by linear dynamics along with nonlinear output. The UKF is another popular version of the Kalman filter that belongs to the sigma-point filter family, and provably offers second-order accuracy under certain conditions, contrasting with the first-order accuracy of the EKF. The proposed SOC estimation methods are validated through simulations and experimental data under various conditions, showing significant accuracy as well as robustness to different levels of initialization error and noise.

Acknowledgements

First, I would like to thank my parents, Terry and Joan, for being constant sources of love and support.

I would also like to thank my sister, Jordan, for her love, friendship, and shared laughter.

To my friends (you know who you are, if you are even reading this) who are more like family;

to Huazhen, for motivating me to strive toward excellence, to fall in love with problems, and teaching me much more than estimation algorithms and about battery technology;

to the ISSL group, who are supportive, kind, and curious;

to my coworkers and supervisors at Spear Power Systems, for the support, guidance, and flexibility; thank you. This would not be possible without you.

Contents

List of Figures

List of Tables

Chapter 1

Introduction

1.1 Background

As the world tends toward electrification, rechargeable batteries have received ever-growing attention as a primary energy storage device. Batteries have a plethora of uses, ranging from consumer electronics such as laptops and cell phones to larger scale systems, such as electric vehicles and grid energy storage. The increasing use of rechargeable batteries has motivated strong research effort in battery management. Effective models are foundational to battery management system (BMS) design. There are different kinds of models: electrochemical models, equivalent circuit models (ECMs), and data-driven models. ECMs are appealing and useful for their distinct advantages, including computational efficiency owing to parsimonious structures and sufficient accuracy in common operating conditions. They can thus find increasing use in future battery management. Because of this, we will consider ECMs in this thesis. Specifically, we will address the problem of state-of-charge (SOC) estimation by using a novel equivalent circuit model (ECM) proposed in [1] along with extended and unscented Kalman filtering.

A literature review of SOC will be given first to aid in understanding the aim of this work, and to provide context about where this work lies in the research community. The SOC of a battery cell is defined as the ratio of available capacity to the total capacity of the cell at present time, and is commonly shown as a percentage value on devices such as cell phones and laptops. To most everyday users, the battery status of their electronic device is taken for granted, but behind this value on the user's screen is an algorithm which is necessary to infer the SOC from current, voltage, and temperature measurements. An accurate SOC knowledge is required in advanced battery

management systems (BMSs), such as those in electric vehicles, for several purposes. In order to avoid overcharge and overdischarge of the batteries [2], which can result in fire or explosion [3], the user or BMS must accurately know the cell charge level. The SOC also acts as a reference to cell balancing strategies, power calculations, and energy calculations [4], such as state-of-power and state-of-health estimates. Poor charging and discharging strategies can reduce the lifetime of a battery; therefore, knowing the SOC can help avoid these problems — it has been shown that a battery cell has significantly longer cycle life when a lower depth-of-discharge (DOD) is used during its operation, within limited SOC bounds, i.e. $SOC_{min} = 20\%$ and $SOC_{max} = 80\%$.

SOC estimation methods can be separated into two groups: traditional model-free methods and more recent but increasingly popular model-based and data-based methods. Traditional methods do not make use of battery models and instead rely on measurements or straightforward calculations. One such ubiquitous method is coulomb counting, where the SOC of a cell is tracked by the integration of current over time. This method is highly reliant on an accurate initial current reading and is subject to drift errors, making it inadequate for advanced battery applications [5]. Another traditional technique is voltage translation, in which an open-circuit-voltage (OCV) measurement is taken and the SOC is found from an SOC-OCV lookup table or curve that was determined offline. This method is cumbersome and impractical due to the rest period needed to accurately measure OCV [6].

Recent methods to estimate SOC make use of either advanced data-driven or physics-based models. Most recently, machine learning methods such as artificial neural networks [7] and support vector machines [8] have been proposed for estimating SOC, where a data-driven predictive model is built by training the battery data sets. One drawback to this method is that extensive offline training is necessary and takes time. In the literature, there are two predominant model-based SOC estimation methods for batteries — electrochemical models or equivalent circuit models. Electrochemical models are capable of characterizing the reaction kinetics, ion transport, and thermodynamics within the battery [9; 10]. Unfortunately, in order to accurately describe the phenomena occurring in the battery, these models use partial differential equations which require complex

computational operations. Generally, electrochemical models are too computationally expensive to be useful in real-time BMS SOC monitoring, which is often implemented on an embedded processing chip [11]. The conversion of these algorithms to embedded code can be quite cumbersome and tedious.

ECMs, however, offer much higher computational efficiency than electrochemical models. ECMs are able to simulate the current-voltage (input-output) behavior of a battery by modeling the battery as an electric circuit with components such as voltage sources, resistors, and capacitors. Using Kirchhoff's Circuit Laws, one can describe the given circuit with a relatively small parameter set and only a few equations. Even with such simplification, ECMs can achieve high accuracy in describing the behavior of batteries. The simplicity and efficacy of ECMs make them great candidates for use in advanced BMSs that require real-time estimation of various battery states, especially SOC [6; 12].

Within the model-based SOC estimation field, there exist nonlinear observers and stochastic estimators. Among the nonlinear SOC observers are Luenberger observers [9], and sliding-mode, adaptive and robust observers [13; 14], which view the battery model as a deterministic system. On the other hand, stochastic estimators possess the ability to suppress the noise that naturally occurs within and affects a dynamic system [6]. The Kalman filter, a recursive and probabilistic estimation technique, is the most notable of this type, which has been used to address a broad range of stochastic estimation problems including robotics, guidance, navigation, control, and signal processing [15]. The extended Kalman filter (EKF) and unscented Kalman filter (UKF) [16] are extensions of the standard Kalman filter for nonlinear systems, which make them attractive suitors for SOC estimation.

1.2   State of the Art

At the moment of the writing of this thesis, there exists a multitude of studies on estimating the SOC of batteries, as referenced in the previous section. A reader may wonder where this work stands in relation to the state-of-the-art and what advantages it possesses. The answer lies in the

modeling approach, and how we can glean more information about the cell operation through the model. In the literature, as stated before, SOC estimation is typically done using electrochemical models or ECMs, which allow the BMS to track either the ionic diffusion between electrodes or follow the current-voltage behavior to infer the charge status of the battery. This thesis, while briefly covering the electrochemical phenomena that occurs within a battery, mainly focuses on using Kalman filtering based on a newly developed ECM to do SOC estimation. Tian, Fang, Chen, and Wang proposed this novel ECM named the Nonlinear Double-Capacitor model in [1]. This work proposes, develops, and verifies a new ECM that is more accurate than previous ECMs. Using this model, we can achieve greater accuracy of SOC and SOH estimation using well-known techniques, such as EKF and UKF.

1.3 Thesis Objective and Contributions

There is an increasing demand for battery systems which require advanced and high-fidelity BMS implementations. The objective of this thesis is to present improved SOC estimation results obtained from using well-known stochastic techniques along with a novel ECM, the NDC model.

This work presents the following contributions:

- Accurate SOC estimation using the novel NDC model based on EKF and UKF algorithms;

- Experimental results to validate the NDC model-based SOC estimation methods.

1.4 Thesis Organization

The rest of the thesis will be arranged as follows. Chapter 2 provides context on battery modeling and introduces the NDC model. Chapter 3 discusses battery state estimation in depth. Chapter 4 describes the experimental setup and presents experimental results. Finally, Chapter 5 concludes the work.

Chapter 2

Battery Modeling

2.1 Preliminaries

In this section, an introduction to batteries is given. The discussion will begin by reviewing the basics of battery operation and use, followed by a brief overview on different types of batteries. Then, the components within batteries are analyzed in detail to gain a deeper understanding of the electrochemistry within a cell. Finally, important parameters, characteristics, and phenomena of batteries are defined, leading into the rest of the chapter which provides a thorough review of various equivalent circuit models.

Batteries are devices that convert stored chemical energy, harnessed from internal electrochemical reactions, to electrical energy. Technically speaking, a cell is the smallest electrochemical component capable of supplying a voltage, while a battery consists of multiple cells connected in series, parallel, or some combination thereof [12]. Most automotive starting, lighting, and ignition batteries, for example, are actually several smaller cells, approximately 2 V each, connected in series to form an approximately 12 V battery. There are also different types of cells, namely primary cells and secondary cells. Primary cells are not rechargeable and can only be used once before the reagent within has run out, and secondary cells are capable of reversible reactions thereby allowing numerous charging and discharging cycles. The focus of this work will be on secondary cells.

Cell categorization is not just limited to rechargeability — they are also grouped based on their shape. Cells are manufactured in various shapes, the most popular being cylindrical cells, prismatic cells, and pouch cells. Cylindrical cells, first introduced in the late 1800s, are one of the most commonly used packaging shapes due to the ease of manufacturing and their durability. The

cylindrical shape allows them to withstand high internal pressure levels [17]. Of the cylindrical cell variety, 18650 is the most popular form factor. The form factor is simply the shape, and 18650 refers to the dimensions of the battery: the diameter is 18mm, the height is 65mm, and the 0 means the shape is cylindrical. Common applications for cylindrical cells include portable electronics, power tools, medical instruments, and sometimes vehicles — Tesla use cylindrical cells for its EVs. Some advantages of cylindrical cells include long lifetime and inexpensive production, while some disadvantages are their high weight and poor packing density (cylinders stacked together will have space cavities, and sometimes these spaces are taken advantage of for cooling purposes). Prismatic cells were first introduced in the 1990s. These cells are manufactured using a layered approach, which allows for optimal spacing in devices and applications [17]. Prismatic cells come in various sizes and can be used in consumer electronics, such as laptops and cell phones, as well as in hybrid vehicles, electric vehicles, and electric powertrains. While prismatic cells are advantageous for spacing purposes, they are more expensive and typically have shorter cycle life than their cylindrical counterparts. Continuing in the thinner direction, we arrive at pouch cells. These were introduced in the 1990s as a lightweight and modular alternative to existing cell shapes. Pouch cells have the highest packing efficiency, around 90% [17], and are often used in military and automotive applications where there is a need for lightweight design. Pouch cells commonly utilize lithium-polymer chemistries, which can provide high energy density. One downfall of pouch cells are their tendency to swell when the electrolyte degrades, or when the cell is overcharged. This can cause dangerous conditions in the battery compartment, because the gases that accumulate in the pouch cell, including carbon dioxide and carbon monoxide, are flammable and poisonous. While the shape of the battery is a very important consideration for applications, the cell chemistry will ultimately dictate the effectiveness of the battery system, namely the energy density and cycle life.

Many types of batteries exist for a plethora of use cases. Among the most common rechargeable battery systems are Nickel Cadmium (NiCd), Nickel-Metal Hydride (NiMH), lead-acid, lithium polymer (LiPo), and lithium ion (Li-ion). NiCd are cheap but have low energy density (typically expressed in watt-hours per kilogram). NiMH have higher energy densities than NiCd with lower

cycle life, and are more environmentally friendly than NiCd. Lead-acid batteries can be used in large power applications, such as deep cycling batteries for grid energy storage [18] and backup power supplies for data server centers. LiPo batteries offer similar performance, which are subsequently discussed, to Li-ion in slim geometries. Finally, we arrive at Li-ion batteries. The Li-ion battery technology enables our omnipresent portable electronics to achieve extremely light weight and slim design, expands the capabilities of electric tools, and powers hybrid and electric vehicles toward more widespread adoption in the automotive industry. These advances are possible due to the high energy density, high cycle life, and low self-discharge rate of Li-ion batteries. Li-ion batteries, while advantageous performance-wise, can be dangerous if used improperly or if the battery management circuitry is faulty — this includes overcharging or overdischarging, which can cause short circuits and even thermal runaway, damaging the battery by crushing, overheating, etc., which can pressurize the flammable electrolyte leading to fire or explosion, or operating outside the voltage range specified by the manufacturer. Although the battery model and estimation algorithms are applicable to numerous chemistries, this work focuses on Li-ion battery applications.

Within a Li-ion cell, there are four main components: the negative electrode, positive electrode, electrolyte, and separator. Additionally, current collectors are attached to each electrode. A schematic of these components is shown in Figure 2.1. Li-ion cells are a special type of cell known as an intercalation cell. This refers to an intercalation mechanism in which the lithium ions (Li^+) migrate between electrodes, and are inserted into crystal lattice or layered structures. This process allows much higher cycle lifetime than other rechargeable cells where reversible reactions take place, because the intercalation mechanism is much less damaging to the active materials in the electrodes than electrochemical reactions. During charging, Li^+ migrate from the positive electrode through the electrolyte and separator to the negative electrode. When the Li^+ reaches the negative electrode, they are inserted into the crystalline lattice structure of the electrode without reacting with the material. While these Li^+ are migrating from the positive electrode to the negative electrode during charging, the electrons, e^-, are traveling through an external connection to reach the negative electrode, as the separator prevents them from freely moving between the electrodes.

This ensures that the Li$^+$ bond with the free e$^-$ in the electrode, so that Li$^+$ exists in the electrolyte and lithium composites exist in the electrodes. When it is time to discharge, the lithium composite gives up an electron and travels as Li$^+$ through the electrolyte from the negative electrode to the positive electrode to be inserted into the lattice of the positive electrode [12].
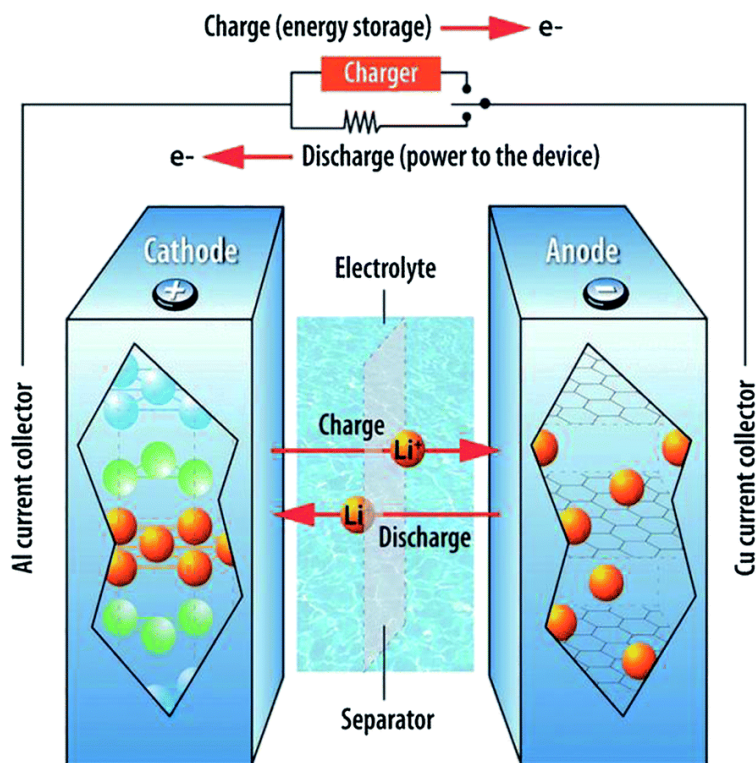
Figure 2.1: Lithium-Ion Battery Schematic. Image courtesy of Argonne National Laboratory

The negative electrode is typically a form of graphite (C_6). This is due to the layered nature of graphite, which contains graphene layers into which lithium can intercalate. Graphite is selected for the active material in the negative electrode because it can withstand thousands of cycles of the reversible electrochemical processes that occur within a battery.

The positive electrode in a Li-ion battery is usually composed of one of three active materials: LCO, LMO, or olivine style phosphates [12]. The first type, LCO, has the molecular formula Li_xCoO_2. LCO compounds have a layered structure, and are used in small electronics. Cobalt is expensive, however, and can be toxic, so sometimes Nickel is substituted in place of Cobalt. Other alternative blends have been used, including Nickel, Cobalt, and Manganese (NCM) and Nickel,

Cobalt, and Aluminum (NCA), each offering different properties. For example, the use of Nickel can increase the energy density of the cell. LCO allows for 2D diffusion of Li^+. The second type of active material, LMO, has the molecular formula $Li_xMn_2O_4$. This category of positive electrodes are cheaper than LCO, but have shorter lifetimes. Lastly, olivine phosphate compounds can also be used for the active material in positive electrodes. The most common compound of this type is Li_xFePO_4 (LFP) due to its safety and low cost, but LFP does not have as much energy density as LMO or LCO. These olivine style phosphates only allow for 1D diffusion of Li^+.

The electrolyte is the ionically conductive solution that enables ion transport between electrodes. This solution consists of a solvent and a solute, consisting of a salt, base, or acid, dissolved in the solvent. Because lithium has a violent reaction with H_2O, Li-ion cells utilize a non-aqueous solvent combined with a lithium salt. The solvents are typically some kind of carbonate, such as ethylene carbonate, diethyl carbonate, or propylene carbonate, while the lithium salt is either $LiPF_6$, $LiBF_4$, or $LiClO_4$.

The separator exists in order to prevent short-circuits, which occur if the negative and positive electrode particles were to come into contact with each other. The separator is permeable and allows Li^+ to pass through, while preventing the two electrode materials to penetrate. The separator is electronically insulated so that the electrons do not pass through, and instead flow through the outer circuit during charging or discharging.

The following list contains a brief description of important concepts, defining characteristics, and phenomena of electrochemical cells [12]. This will aid in understanding the following discussion regarding ECMs.

Ohmic resistance: The voltage of a cell drops when connected to a load, and the ohmic resistance refers to the opposition of current flow in a circuit. This is the resistance that naturally occurs when a current flows through the metal circuitry in the battery.

Ionic resistance: Ionic resistance represents the opposition of current by chemical processes within the battery, such as the surface area of the electrode and the conductivity of the electrolyte.

Polarization: Polarization is a broad term, but can be understood in this context as any difference

in the cell's terminal voltage relative to the OCV when a current is passed through the circuit.

Rate capacity effect: When discharging a battery with high current, the voltage drops faster which indicates a reduction in effective capacity. This is named the rate capacity effect, because the discharge rate affects the capacity of the cell.

Recovery effect: If the current is cut off intermittently during discharge, it can be seen that the voltage increases, or recovers, during the unloaded condition.

SOC-OCV relationship: The relationship between the charge state and the OCV of the battery depends on the chemistry used in the positive and negative electrodes. This relationship is nonlinear and is a defining characteristic of batteries. Accurately modeling the SOC-OCV relation is crucial for BMSs.

Hysteresis: A cell's voltage will be different during charging and discharging, i.e., at the same SOC value the voltage is higher during charging than during discharging. It is important to note the difference between hysteresis and diffusion voltages — hysteresis is a function of the recent charging and discharging history, along with the SOC, while diffusion voltage is a function of time and will decay to OCV [12].

Battery modeling is generally separated into two categories: electrochemical models and equivalent circuit modeling. Electrochemical models characterize the phenomena occurring inside the battery cell, such as ion migration and diffusion processes, while ECMs focus on capturing the input-output behavior of batteries using circuits. The focus of this thesis will be on the latter due to the low dimensionality, modeling accuracy, and computational efficiency offered by ECMs, and thus we omit in-depth discussion of electrochemical models.

2.2 Equivalent Circuit Modeling

Rather than attempt to model the complex physical phenomena occurring within a battery like electrochemical models, ECMs seek to reconstruct the input-output, i.e., current-voltage, behavior of the battery using electrical circuits consisting of voltage sources, resistors and capacitors in varying configurations. ECMs generally contain fewer states and parameters than other modeling

approaches which make them good candidates for online estimation tasks. In this section, the discussion of ECMs will be built up from the 1940s, when Randles proposed the first known ECM [19], to present day, where a variety of ECMs have been developed and are continually being improved upon.

2.2.1 Randles' Model

The Randles' model was the first ECM and was originally used to model lead-acid batteries [20]. The applications have been extended to various battery types, including Li-ion batteries. The Randles' model, shown in Figure 2.2, makes use of two capacitors, C_b and C_s, to model the OCV and the diffusion processes within the battery, respectively. More specifically, C_b is used to represent the bulk charge storage of a cell and the voltage across this capacitor, V_b, represents the OCV. The C_s capacitor is used to represent the double-layer effect of the electrode-electrolyte boundary. Several resistors are used to capture the various resistances encountered within a cell: R_s represents the series resistance, R_d represents the cell's self-discharge, and R_t models the charge-transfer resistance.

$$\begin{bmatrix} \dot{V}_b(t) \\ \dot{V}_s(t) \end{bmatrix} = \begin{bmatrix} \frac{-1}{C_b R_d} & 0 \\ 0 & \frac{-1}{C_s R_t} \end{bmatrix} \begin{bmatrix} V_b(t) \\ V_s(t) \end{bmatrix} + \begin{bmatrix} \frac{1}{C_b} \\ \frac{1}{C_s} \end{bmatrix} I(t) \tag{2.1a}$$

$$V(t) = V_b + V_s + I(t)R_s \tag{2.1b}$$

Note that the sign of the current, I, is positive $(+)$ for charge and negative $(-)$ for discharge. This will be the convention used throughout the following discussion, unless otherwise noted.

2.2.2 Rint Model

The next ECM to review is the Rint model, also known as the internal resistance model. The Rint model, as shown in Figure 2.3, consists of an ideal voltage source V_{OC} and a resistor connected in series, R_s. The ideal voltage source represents the cell's OCV and the serial resistor represents the

Figure 2.2: Randles' circuit model.
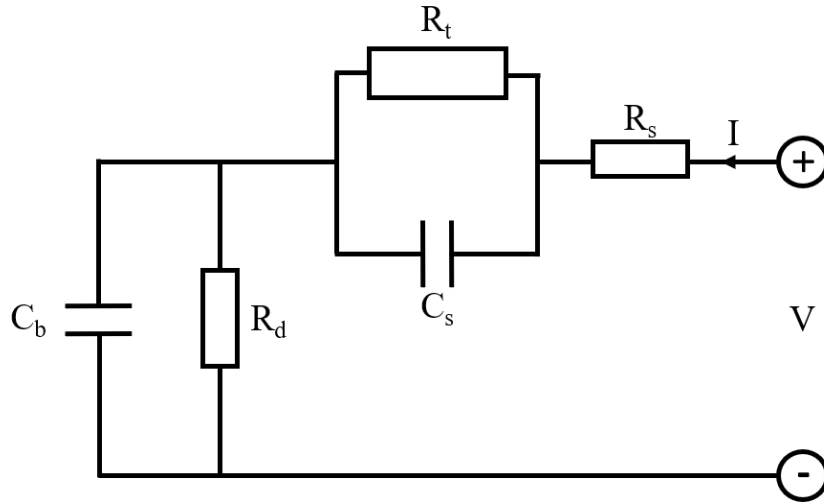
internal resistance of the cell. The terminal voltage can be described by the following equation:
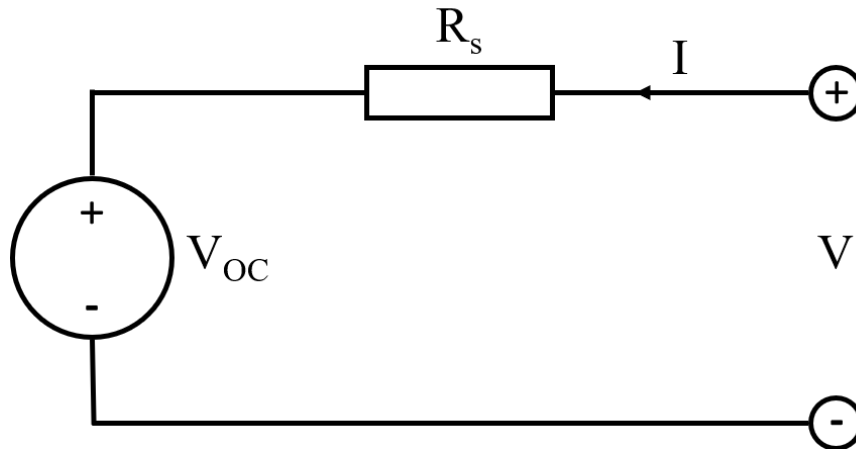
$$V(t) = V_{OC} + I(t)R_s \tag{2.2}$$

Figure 2.3: Rint circuit model.

2.2.3 Thevenin's Model

The Thevenin model is a modified version of the Rint model, with a parallel R-C branch added in series with the voltage source and resistor. Multiple R-C branches may be added to increase

12

modeling accuracy, at the cost of higher computational complexity. In the Thevenin model, the voltage source represents the OCV of the cell, the resistor R_o represents the polarization resistance, and the parallel R-C branch is used to model the transients caused by the diffusion of ions into the electrolyte. The voltage across the R-C branch is V_{Th}. The model is characterized by:
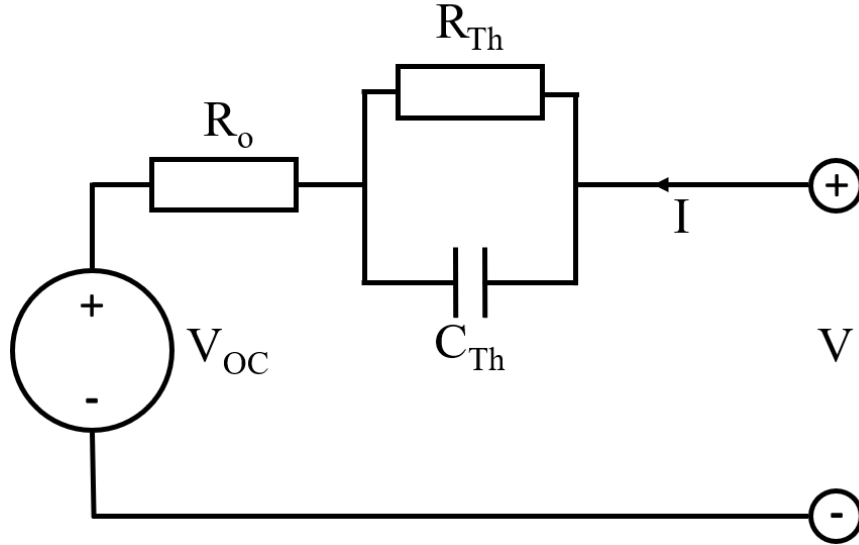
Figure 2.4: Thevenin circuit model.

$$\dot{V}_{Th}(t) = -\frac{V_{Th}(t)}{R_{Th}C_{Th}} + \frac{I(t)}{C_{Th}} \tag{2.3a}$$

$$V(t) = V_{OC} + V_{Th}(t) + I(t)R_o \tag{2.3b}$$

One can further expand the model by adding SOC as another state variable and letting V_{OC} be SOC-dependent. This modification accounts for the SOC-OCV relationship, thus leading to higher modeling accuracy.

2.2.4 Double-Capacitor Model

Next, the double-capacitor model makes use of parallel capacitors, allowing the model to characterize lithium-ion diffusion within the electrode of the battery [21; 22]. Each R-C branch represents a region of the electrode. Based on the single particle model (SPM), the R_b-C_b circuit represents

13

the bulk central portion of the electrode with slower diffusion dynamics, and the R_s-C_s circuit represents the surface region of the electrode which is in contact with the electrolyte, where faster ionic diffusion occurs [23; 24]. The double-capacitor model is able to characterize the rate capacity effect, capacity recovery effect, and voltage recovery effect.

Typically, the voltages across the two capacitors are taken as the states of the model, but one may wish to write the model equations in terms of the charge stored in each capacitor if the application calls for it. In this thesis, we will look at the more common scenario where the voltages across the C_b and C_s capacitors, V_b and V_s respectively, are the states of interest.
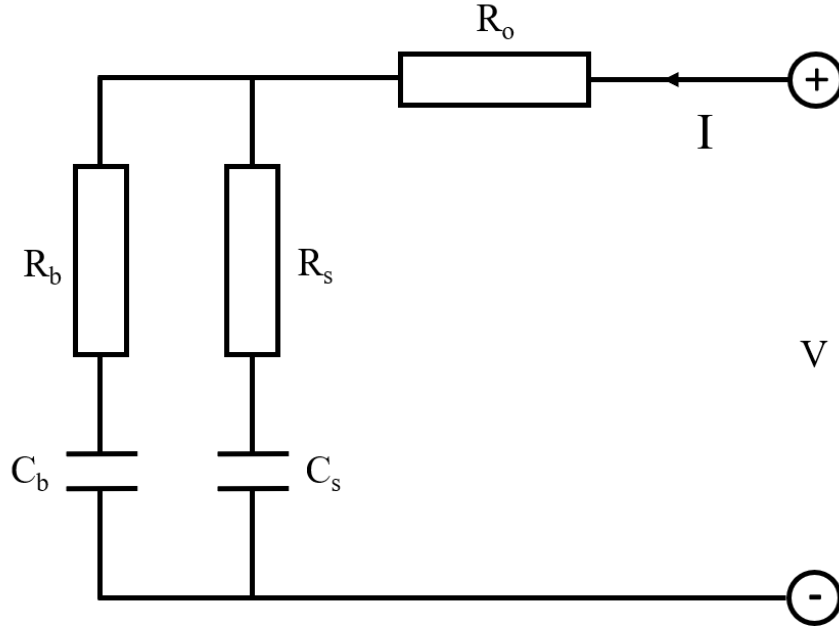
Figure 2.5: Double-capacitor model.

$$
\begin{bmatrix} \dot{V}_b(t) \\ \dot{V}_s(t) \end{bmatrix} = \begin{bmatrix} \frac{-1}{C_b(R_b+R_s)} & \frac{1}{C_b(R_b+R_s)} \\ \frac{1}{C_s(R_b+R_s)} & \frac{-1}{C_s(R_b+R_s)} \end{bmatrix} \begin{bmatrix} V_b(t) \\ V_s(t) \end{bmatrix} + \begin{bmatrix} \frac{R_s}{C_b(R_b+R_s)} \\ \frac{R_b}{C_s(R_b+R_s)} \end{bmatrix} I(t) \tag{2.4a}
$$

$$
V(t) = \begin{bmatrix} \frac{R_s}{R_b+R_s} & \frac{R_b}{R_b+R_s} \end{bmatrix} \begin{bmatrix} V_b(t) \\ V_s(t) \end{bmatrix} + \begin{bmatrix} R_o + \frac{R_bR_s}{R_b+R_s} \end{bmatrix} I(t) \tag{2.4b}
$$

14

2.3 Nonlinear Double-Capacitor Model

In this section, the NDC model is introduced, and an overview of the motivation for its development and the mathematical equations characterizing its behavior are presented.

The NDC model is an extension of the double-capacitor model, as in [21; 22]. The motivation for extending the double-capacitor model stems from the linear nature of the model. Because a battery's behavior is nonlinear, namely the SOC-OCV relationship, the double-capacitor model is unable to account for the nonlinearities of the OCV at low and high SOC values. The double-capacitor model, therefore, is limited to confined SOC ranges for which a linear approximation of the OCV dependency on SOC is suitable. The NDC model was proposed to address this limitation, and was initially presented in a conference paper [25], and complete results are shown in [1]. The two modifications to the double-capacitor model are as follows:

- A voltage source U was introduced as a nonlinear mapping of V_s, $U = h(V_s)$, because the OCV depends heavily on the concentration of lithium ions in the surface region in the SPM model, which allows the NDC model to account for the nonlinear SOC-OCV relationship.

- An RC circuit, R_1-C_1, was added in series to the new voltage source and the ohmic resistance R_0 to characterize the voltage transients at the electrode-electrolyte interface.

The NDC circuit model is shown in Figure 2.6.

The dynamics of the NDC model, in state-space form, are shown as follows.

$$\begin{bmatrix} \dot{V}_b(t) \\ \dot{V}_s(t) \\ \dot{V}_1(t) \end{bmatrix} = A \begin{bmatrix} V_b(t) \\ V_s(t) \\ V_1(t) \end{bmatrix} + BI(t) \tag{2.5a}$$

$$V(t) = h(V_s(t)) - V_1(t) + R_0 I(t) \tag{2.5b}$$
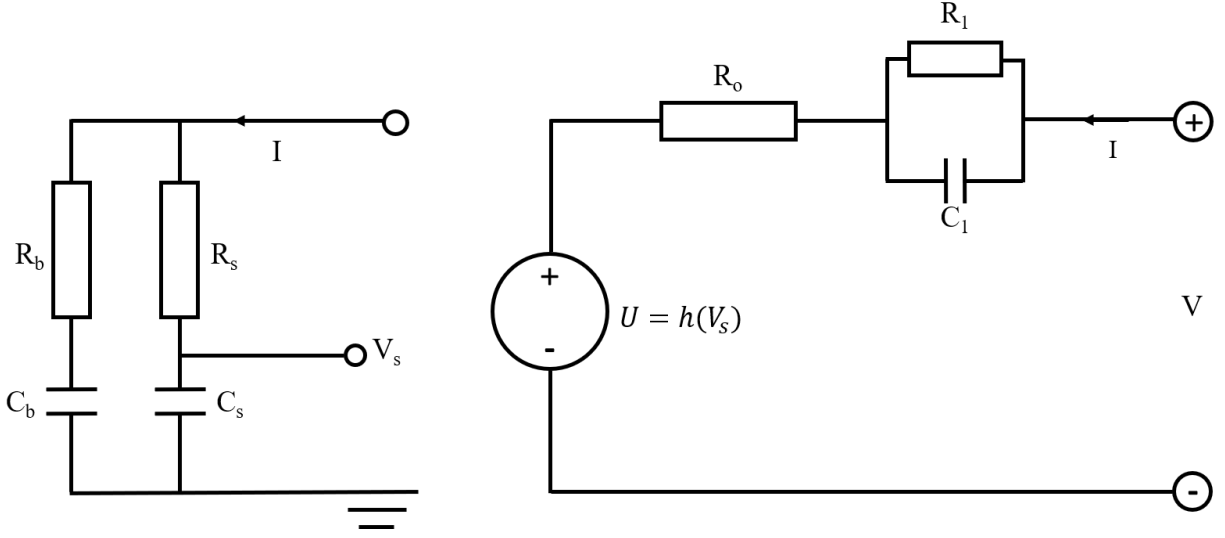
Figure 2.6: The nonlinear double-capacitor model.

where

$$
A = \begin{bmatrix} \frac{-1}{C_b(R_b+R_s)} & \frac{1}{C_b(R_b+R_s)} & 0 \\ \frac{1}{C_s(R_b+R_s)} & \frac{-1}{C_s(R_b+R_s)} & 0 \\ 0 & 0 & \frac{-1}{R_1C_1} \end{bmatrix} , \ B = \begin{bmatrix} \frac{R_s}{C_b(R_b+R_s)} \\ \frac{R_b}{C_s(R_b+R_s)} \\ \frac{-1}{C_1} \end{bmatrix}
$$

The NDC formulation assumes that the voltages across the two capacitors, V_b across C_b and V_s across C_s, are bounded by [0, 1] V. The implication of this assumption is that at a full charge of 100% SOC, $V_b = V_s = 1$ V, and at 0% SOC, $V_b = V_s = 0$ V. The SOC is then defined by the following equation:

$$
\text{SOC} = \frac{Q_a}{Q_t} = \frac{C_b V_b + C_s V_s}{C_b + C_s} \times 100\% \tag{2.6}
$$

In Equation (2.6), Q_a is the available capacity of the cell and Q_t is the total capacity of the cell. In the nonlinear measurement equation shown in Equation (2.5), the $h(V_s)$ term can be parameterized as a fifth-order polynomial and is written as

$$
h(V_s) = \alpha_0 + \alpha_1 V_s + \alpha_2 V_s^2 + \alpha_3 V_s^3 + \alpha_4 V_s^4 + \alpha_5 V_s^5 \tag{2.7}
$$

16

and the internal resistance, R_0, is SOC dependent and is described by the following equation:

$$R_0 = \gamma_1 + \gamma_2 e^{-\gamma_3 \text{SOC}} + \gamma_4 e^{-\gamma_5(1-\text{SOC})} \tag{2.8}$$

In order to use the NDC model for battery modeling and estimation, we need an explicit form. To achieve this, it is important to note that

$$\text{OCV} = h(\text{SOC}) \tag{2.9}$$

and this SOC-OCV relationship described by $h(\cdot)$ must be determined, as well as the impedance and capacitance parameters. The following section presents the methods and results regarding parameter identification of the NDC model.

2.4 Parameter Identification

Now that we have a model structure with unknown parameters, we can begin the parameter identification procedure which will allow us to obtain an explicit model for use. The identification method shown here follows that of [1]. The NDC model contains two sets of parameters, α and β. First, the parameter set α describing the SOC-OCV relation via the $h(\cdot)$ function will be determined where α is defined as

$$\alpha = \begin{bmatrix} \alpha_0 & \alpha_1 & \alpha_2 & \alpha_3 & \alpha_4 & \alpha_5 \end{bmatrix}^T \tag{2.10}$$

As is common in the literature, we use a trickle current discharge of 1/30 C so that the terminal voltage of the battery, V, can be approximated as the OCV. Using the input and output data obtained from the aforementioned discharge, we can solve the following linear least squares problem:

$$V = Z\alpha \tag{2.11}$$

where

$$Z = \begin{bmatrix} 1 & \text{SOC} & \text{SOC}^2 & \text{SOC}^3 & \text{SOC}^4 & \text{SOC}^5 \end{bmatrix} \tag{2.12}$$

to determine the parameter set α which describes the SOC-OCV relationship. The solution is the well-known ordinary least squares (OLS) estimator

$$\hat{\alpha} = (Z^T Z)^{-1} Z^T V \tag{2.13}$$

where the SOC values are obtained via coulomb counting

$$\text{SOC}(t) = \text{SOC}(t-1) + \frac{I(t)}{Q_t} \Delta t \tag{2.14}$$

with Q_t as the total capacity of the battery determined by the amount of charge supplied from full to empty, i.e., a discharge from SOC = 1 to SOC = 0. Using MATLAB, we can import the discharging data, namely the measured terminal voltage, to find the parameter set by fitting a fifth order polynomial to the SOC-OCV curve.

Now that the SOC-OCV relation has been determined, we can identify the impedance and capacitance parameters. Rather than a trickle discharge current, we now wish to discharge the cell using a 1C discharge rate. This larger magnitude input stimulus will trigger a response from the cell, enabling the impedance and capacitance parameters to be identified. Also, because a 1C discharge rate is in the middle of the operating range of the cell, identifying the model using this current rate will give us an accurate depiction of the cell dynamics.

The parameter identification approach here is to derive an explicit form of the terminal voltage equation in terms of a parameter set, β, containing the impedance and capacitance parameters, and to minimize the difference between the voltage predicted by this derived equation and the measured voltage of the 1C discharge test. If we look at the terminal voltage measurement equation, $V(t) = h(V_s(t)) - V_1(t) + R_0 I(t)$, we can see it contains V_s and V_1 from the state, along with R_0. The solution to a state space equation, given by Chen in [26], will be used to find expressions for V_s

18

and V_1, and R_0 is given in terms of the parameter set γ and SOC, as derived in [1].

First, V_s will be explicitly determined. According to [26], the solution to a linear time-invariant (LTI) state space equation can be explicitly shown. Consider the general LTI state-space state equation

$$\dot{x}(t) = Ax(t) + Bu(t) \tag{2.15}$$

where A and B are constant matrices, invariant in time. In system theory, the response of the system to excitation is analyzed in two parts: initial conditions and input. It is apparent in the solution below that $x(0)$ and $u(t)$ play a role in the system response. The solution to Equation (2.15) is

$$x(t) = e^{At}x(0) + \int_0^t e^{A(t-\tau)}Bu(\tau)d\tau \tag{2.16}$$

where e^{At} can be solved using the Cayley-Hamilton theorem.

The next steps are to substitue the matrix exponential term e^{At} into Equation (2.16) and solve the integral representing the response of the system to the input. The following explicit representations of V_s and V_1 are given as follows:

$$V_s(t) = V_s(0) + \frac{It}{C_b + C_s} + \frac{C_b(R_bC_b - R_sC_s)I}{(C_b + C_s)^2} \cdot \left[1 - \exp(-\frac{C_b + C_s}{C_bC_s(R_b + R_s)}t)\right] \tag{2.17}$$

$$V_1(t) = e^{\frac{-t}{R_1C_1}}V_1(0) - IR_1(1 - e^{\frac{-t}{R_1C_1}}) \tag{2.18}$$

It is important to keep in mind that these are needed because they are the states that appear in the NDC model's measurement equation. We wish to minimize the difference between the measured terminal voltage of a cell and the model's prediction of the terminal voltage — we can infer the parameters if the model's predicted terminal voltage is written in terms of the parameter set. It should be noted that the term $1/(C_b + C_s)$ can be determined prior by using coulomb counting. With this goal in mind, the explicit forms of V_s and V_1 are given in terms of the parameter set below:

$$V_s(t, \beta) = V_s(0) + \frac{It}{C_b + C_s} + \psi_1 I(1 - e^{-\psi_2 t}) \tag{2.19}$$

19

$$V_1(t, \beta) = e^{-\psi_4 t} V_1(0) - I\psi_3(1 - e^{-\psi_4 t}) \tag{2.20}$$

where the parameter set β is defined as follows:

$$\beta = \begin{bmatrix} \psi_1 & \psi_2 & \psi_3 & \psi_4 & \gamma_1 & \gamma_2 & \gamma_3 & \gamma_4 & \gamma_5 \end{bmatrix}^T \tag{2.21}$$

where $\psi_1 = \frac{R_b C_b^2}{(C_b + C_s)^2}$, $\psi_2 = \frac{C_b + C_s}{C_b C_s R_b}$, $\psi_3 = R_1$, $\psi_4 = (R_1 C_1)^{-1}$, and $\gamma_1, \gamma_2, \dots, \gamma_5$ are the parameters describing the SOC dependent R_0 relationship shown in Equation (2.8).

Now, we can write the model's predicted terminal voltage as a function of these state expressions

$$V(t, \beta) = \sum_{i=0}^{5} \alpha_i V_s^i(t, \beta) + I\beta_5 + I\beta_6 e^{-\beta_7 \text{SOC}} + I\beta_8 e^{-\beta_9(1-\text{SOC})} + I\beta_3(1 - e^{-\beta_4 t}) \tag{2.22}$$

The minimization problem below is formulated to solve for the parameter set β by minimizing the difference between the measured terminal voltage vector set y and the voltage values predicted by the model, $V(\beta)$

$$\hat{\beta} = \arg\min_{\beta} \frac{1}{2} [y - V(\beta)]^T R^{-1} [y - V(\beta)] \tag{2.23}$$

$$\text{s.t.} \underline{\beta} \leq \beta \leq \overline{\beta}.$$

In this formulation, $\hat{\beta}$ is the estimated parameter set, y is the set of measured terminal voltages of length N, in vector form, $V(\beta)$ is the set of model predicted terminal voltages shown in Equation (2.22), and R is an $N \times N$ measurement noise covariance matrix.

Since we know the parameter sets α and β describing the SOC-OCV relationship and the RC parameters, the NDC model is explicitly available and ready for use.

2.5   Chapter Summary

This chapter builds from the basic phenomena occurring within batteries, and the components therein, to an explicit model of a battery. There exists a plethora of electrochemistries able to supply a voltage, and each type has unique internal processes and input-output behavior. Modeling these battery dynamics, as discussed before, can be done using electrochemical models or ECMs. This work focuses on the latter, ECMs, specifically the NDC model. The following chapters will include using this model as a basis for estimating SOC, under various cases, with the EKF and UKF, along with simulated and experimental validation.

Chapter 3

Battery State Estimation

3.1 Introduction

Once we have a model that is able to accurately characterize the dynamics of a cell, we can apply a plethora of different techniques in order to achieve estimation tasks, and because the primary task of a BMS is to provide real-time SOC information of the cell, we are interested in model-based SOC estimation. Nonlinear observers and stochastic estimators are popular choices for SOC estimation, and in this work we will utilize stochastic estimators. The noise that naturally occurs within a system, affecting its dynamics, can be suppressed by these stochastic techniques, which make them an appealing choice for SOC estimation. A notable stochastic estimation method is the Kalman filter, which is a recursive algorithm that is used in a wide range of estimation problems and applications [15]. The Kalman filter was proposed in 1960 by Rudolf Kalman, and in its base form is the optimal estimator for linear systems. There are several nonlinear extensions which achieve great and competitive performance for nonlinear systems, though they may be theoretically sub-optimal. Of the nonlinear extensions, two will be considered in this thesis: the EKF and UKF. This chapter is based, in part, on the work presented in [27].

3.2 Extended Kalman Filter

The EKF linearizes the nonlinear system around the most recent state estimate at each time instant, and then applies the Kalman filter to the linearized model to generate the current state estimate. The filter propagates this new state estimate through the EKF recursion to be used for state estimation at

the next time step. This process continues recursively through time, generating new state estimates at each time instant. For linearization, the Taylor series expansion is considered, and the model is linearized about the most recent state estimate. This state estimate is the conditional mean of the random variable considered to be the state variable given the measurement data. The EKF algorithm will provide first-order accuracy for the state estimate. There will be truncation error becuase the EKF uses a truncated form of the Taylor series, which means the estimates will be sub-optimal [16]. Despite this fact, the EKF remains one of the most used nonlinear estimation methods due to its ease of implementation and practical success. The EKF has been used extensively in the literature for SOC estimation. The EKF was shown to estimate the SOC in electric drive vehicles in [28] with better accuracy than coulomb counting. An adaptive form of the EKF, known as an adaptive extended Kalman filter (AEKF), was implemented in [29]. In [30; 31], another EKF-based SOC estimation method was developed to estimate the SOC when the parameters of the battery model are unknown. An AEKF was used in [32] that employed a covariance matching approach to estimate SOC. In [33], an EKF was implemented to estimate the SOC of lead-acid batteries in hybrid-electric vehicles. A dual EKF was applied in [20] to the most common lumped-parameter ECMs in lithium-ion battery energy storage applications. The EKF is very amenable to design and has become a very popular choice for SOC estimation. Its ability to work for various systems and its relatively low computational complexity have been driving factors for the EKF's ascent in popularity, especially for low-dimensional systems such as an ECM for batteries.

The EKF is performed in three steps: *initialization*, *state prediction (time update)*, and *state update (measurement update)*.

Consider the general discrete-time nonlinear system:

$$
\begin{cases}
x_{k+1} = f(x_k, u_k) + w_k \\
y_k = g(x_k, u_k) + v_k
\end{cases}
\tag{3.1}
$$

where w_k is added to represent the process noise and assumed to be a white Gaussian noise se-quence with the distribution $w_k \sim \mathcal{N}(0, Q)$, and v_k is added to capture the measurement noise

23

which is also considered a white Gaussian noise sequence, where $v_k \sim \mathcal{N}(0, R)$. We begin by initializing the state estimate mean and state estimate covariance:

$$\hat{x}_0 = \mathrm{E}[x_0]$$

$$P_0^x = \mathrm{E}[(x_0 - \hat{x}_0)(x_0 - \hat{x}_0)^T]$$

The state is represented as a random vector whose conditional probability distribution is approximated by $x_k|Y_{k-1} \sim \mathcal{N}(\hat{x}_{k|k-1}, P_{k|k-1}^x)$, where Y_{k-1} is the set of measurements up to time $k-1$, $\hat{x}_{k|k-1}$ is the estimate of x_k given Y_{k-1}, and $P_{k|k-1}^x$ is the covariance of the state estimate at time k given Y_{k-1}. These statistics, i.e., the mean and covariance of the distribution, are then propagated through the time update and measurement update steps as shown below.

State Prediction (Time Update)

$$\hat{x}_{k|k-1} = f(\hat{x}_{k-1}, u_{k-1})$$

$$P_{k|k-1}^x = F P_{k-1|k-1}^x F^T + Q$$

where F is the Jacobian matrix of the nonlinear state function $f(\cdot)$ with respect to the state vector x. When the new measurement y_k is made available, the filter can update its knowledge of the state x_k at time k by approximating the distribution $x_k|Y_k \sim \mathcal{N}(\hat{x}_{k|k}, P_{k|k}^x)$, which is accomplished in the next procedure.

State Update (Measurement Update)

$$\hat{x}_{k|k} = \hat{x}_{k|k-1} + P_{k|k-1}^x \bar{G}_k^T (\bar{G}_k P_{k|k-1}^x \bar{G}_k^T + R)^{-1} [y_k - \bar{g}(\hat{x}_{k|k-1})] \tag{3.2}$$

$$P_{k|k}^x = P_{k|k-1}^x - P_{k|k-1}^x \bar{G}_k^T (\bar{G}_k P_{k|k-1}^x \bar{G}_k^T + R)^{-1} \bar{G}_k P_{k|k-1}^x \tag{3.3}$$

The time update and measurement update steps are repeated for the length of the time series. In the above equations, $\bar{G}_k$ is the Jacobian matrix of $\bar{g}$ around $\hat{x}_{k|k-1}$, defined as the partial derivative of the measurement equation with respect to the latest state estimate, $\hat{x}_{k|k-1}$.

Now that a general framework for the EKF has been shown, consider the NDC discrete-time system, originally shown in Equation (2.5):

$$\begin{cases} x_{k+1} = Ax_k + Bu_k + w_k \\ y_k = g(x_k, u_k) + v_k \end{cases} \tag{3.4}$$

where u_k is the input current I at time k. Because the state dynamics of the NDC model are linear, we can use the discretized form of the state and input matrices, A and B, respectively, in the time update and state update steps. For the measurement update step, we must compute the Jacobian matrix $\bar{G}_k$:

$$\bar{G}_k = \left.\frac{\partial \bar{g}}{\partial x}\right|_{\hat{x}_{k|k-1}} = \begin{bmatrix} (-\gamma_2\gamma_3 e^{-\gamma_3 S\hat{O}C} + \gamma_4\gamma_5 e^{-\gamma_5(1-S\hat{O}C)})I(k)\frac{C_b}{Q_t} \\ \frac{\partial h(\hat{V}_s)}{\partial x} + (-\gamma_2\gamma_3 e^{-\gamma_3 S\hat{O}C} + \gamma_4\gamma_5 e^{-\gamma_5(1-S\hat{O}C)})I(k)\frac{C_s}{Q_t} \\ -1 \end{bmatrix}^T \tag{3.5}$$

where

$$S\hat{O}C = \frac{C_b\hat{V}_b + C_s\hat{V}_s}{C_b + C_s}$$

$$\frac{\partial h(\hat{V}_s)}{\partial x} = \alpha_1 + 2\alpha_2\hat{V}_s + 3\alpha_3\hat{V}_s^2 + 4\alpha_4\hat{V}_s^3 + 5\alpha_5\hat{V}_s^4$$

Using these equations in an iterative process, we may proceed to do SOC estimation.

The EKF provides an appealing choice for SOC estimation based on the NDC model. First, whichever filter we use will be implemented in an embedded system with limited computational resources. The EKF is a good choice for this application to the NDC model, as the model is three-dimensional and the EKF is competitive in computational complexity and convergence for low-dimensional systems [16]. In particular, the EKF has computational complexity of $O(n_x^3)$, where n_x is the dimensionality of the considered system. Equivalent circuit models for batteries tend to be low-dimensional. For example the NDC model has $n_x = 3$, making the EKF well-suited for the task of SOC estimation using this model. Another reason for choosing the EKF is that it

25

Table 3.1: NDC model parameters.

C_b	C_s	R_b	R_s	R_1	C_1
10037	973	0.019	0	0.02	3250
[F]	[F]	[Ω]	[Ω]	[Ω]	[F]

allows for easy tuning for most low-dimensional systems. With the EKF, we only have to tune the Q and R matrices. The measurement noise, represented in R, can be found from the root-mean-squared (RMS) noise values specified by the measurement device, so we are mostly concerned with the selection of Q, which characterizes our confidence in the process model and does not represent any real physical process. For the NDC model, only the measurement equation is nonlinear and the computation of the Jacobian is straightforward.

3.2.1 EKF Simulation Results

In this section, simulation results are presented to validate the effectiveness of applying the EKF to the NDC battery model to estimate SOC (NDC-EKF-SOC). To evaluate the robustness of the EKF against varying initialization errors and noise levels, various simulation conditions were designed and performed based on combinations of three factors: initialization error, the process noise covariance matrix Q and the measurement noise covariance matrix R. Each factor can assume one of two modes. The SOC initialization error is either low at 5% or high at 20%, the process noise covariance matrix is either $Q = 10^{-8}I_3$ or $Q = 10^{-5}I_3$ (where I_3 denotes the identity matrix of dimension three), and the measurement noise covariance matrix R is either $R = 2.5 \times 10^{-6}$ or $R = 0.05^2$. Table 3.2 outlines the eight cases considered in the simulation setting. For this method to be applicable in general practice, it needs to be robust to SOC initialization error because the BMS may not always know the initial SOC of the cell in question, and it needs to be able to adequately track the SOC in the case of large process and measurement noise levels. This simulation design addresses these concerns in each possible combination. The parameter set used for the simulations is given in Table 4.1.

Furthermore, to show the NDC-EKF-SOC algorithm's robustness, the Urban Dynamometer Drive Schedule (UDDS) profile [34] is used as the input current and can be seen in Figure 3.1. The UDDS profile is used by the EPA to evaluate emissions standards in vehicles, and is commonly used in the battery field to verify estimation algorithms due to its rapidly fluctuating design. The rapidly fluctuating profile originates from the velocity measurements of a car in an urban environment, undergoing frequent stops and starts in traffic. For battery testing, these velocity values, given in miles per hour, are transformed to current values in amperes. In these simulations, the profile is scaled to +/- 3 A and begins in a discharge mode for 25 minutes and then switches to a charging mode for the remaining 25 minutes. The sharp change in sign of current (negative during discharge to positive during charge) may cause divergence in estimation algorithms in real-world applications, so it is an important consideration when designing and verifying an SOC estimation algorithm — after all, a secondary battery must be able to both discharge its energy and recharge during its lifetime.

In order to quantify the ability of the proposed algorithm to track the SOC, error metrics must first be defined. The error metrics used to determine the estimation accuracy are defined as follows:

- Root Mean Squared Error (RMSE)

$$\text{RMSE} = \sqrt{\frac{1}{N} \sum_{k=1}^{N} (z_k - \hat{z}_k)^2} \tag{3.6}$$

- Mean Absolute Error (MAE):

$$\text{MAE} = \frac{1}{N} \sum_{k=1}^{N} |z_k - \hat{z}_k| \tag{3.7}$$

- Maximum Error (ME):

$$\text{ME} = \max |z_k - \hat{z}_k| \tag{3.8}$$

where N is the number of samples, z_k is the kth SOC observation and $\hat{z}_k$ is the "kth" SOC estimate.

The RMS error is typically the error metric of choice for estimation schemes, and it computes the standard deviation of the residuals, which are the estimation errors at each time instant. The mean absolute error (MAE) is a widely used metric of forecast error in time series analysis, and is included here for completeness. The maximum error (ME) reports the largest prediction error throughout the entire test. This metric will show the worst case, where the estimated SOC is the furthest from the truth.

Based on the EKF simulation results, we find that the proposed method has considerable robustness to different levels of initialization errors and noise levels. This robustness will make the method advantageous in real-world applications. The EKF is able to accurately track the SOC of the battery and converge quickly, even under large noise and initialization error conditions. The results of the EKF simulations are summarized in Table 3.3, and four cases are plotted in Figures 3.2, 3.4, 3.6, and 3.8, along with their respective estimation error plots. These figures show the benchmark SOC, determined by coulomb counting and referred to as true SOC in sequel, and the estimated SOC along with a 2-σ shaded error region (bound). Note that the so-called 2-σ bound is an approximate quantification of the estimation error covariance in the EKF case. The shaded error region approximately represents two standard deviations away from the mean value (the SOC estimate) — this means that approximately 95.45% of the values should lie within this region. As shown in the figures, this region becomes smaller over time, which represents the decreasing magnitude of the estimation covariance matrix, which in turn represents the increased confidence in the SOC estimate. Most of the true SOC values lie within the shaded error region, and it is apparent in the zoomed-in portion of the figures (from 0 to 150 seconds) that the estimation converges quickly, typically within one to two minutes.

The cases with low process noise are shown, which indicates a high level of confidence in the NDC model's process equation to describe the dynamics of the cell. Both modes, high and low, are shown for initialization error and measurement noise. This is done to emulate a real-world setting, where 1) the BMS may not have accurate state information when the estimation method is initialized and 2) the system may be inherently noisy, such as a battery or cell operating in

Table 3.2: Simulation test design.

Test #	Initialization Error	Process Noise Level	Measurement Noise Level
1	5%	$10^{-5}I_3$	0.05^2
2	5%	$10^{-5}I_3$	2.5×10^{-6}
3	5%	$10^{-8}I_3$	0.05^2
4	5%	$10^{-8}I_3$	2.5×10^{-6}
5	20%	$10^{-5}I_3$	0.05^2
6	20%	$10^{-5}I_3$	2.5×10^{-6}
7	20%	$10^{-8}I_3$	0.05^2
8	20%	$10^{-8}I_3$	2.5×10^{-6}

a marine vessel next to high power converters and other equipment, and the sensors on the cell would return noisy voltage measurements. In Figure 3.2, the NDC-EKF-SOC method is shown to converge around 100 seconds into the simulation, as can be seen in the zoomed-in snapshot at the top of the figure. The true SOC value is within the 2-σ bound of the estimated SOC throughout the duration of the simulation, meaning we can proceed with confidence in our SOC estimation in this setting. The NDC-EKF-SOC method is shown to converge even faster in Figure 3.4, and does so around 25 seconds into the simulation. This follows, because there is less measurement noise in this test setting. As in test setting #3, the true SOC value is within the 2-σ region of the estimated SOC throughout the duration of the simulation, meaning we can proceed with confidence in our SOC estimation. Even with an initialization error of 20%, the NDC-EKF-SOC method converges around 120 seconds into the simulation, shown in Figure 3.6. The true SOC value is within the 2-σ region of the estimated SOC throughout the duration of the simulation. In Figure 3.8, the NDC-EKF-SOC method is shown to converge 30 seconds into the simulation, after compensating for the 20% initialization error. The true SOC value is within the 2-σ region of the estimated SOC throughout the duration of the simulation for this test setting as well.

The SOC estimation error for the EKF simulations is shown in Table 3.3. Three error metrics are reported: RMSE, MAE, and ME. The RMSE values are low in most cases indicating good performance, except for test #2 and #6 which show the largest errors. Throughout all EKF simu-
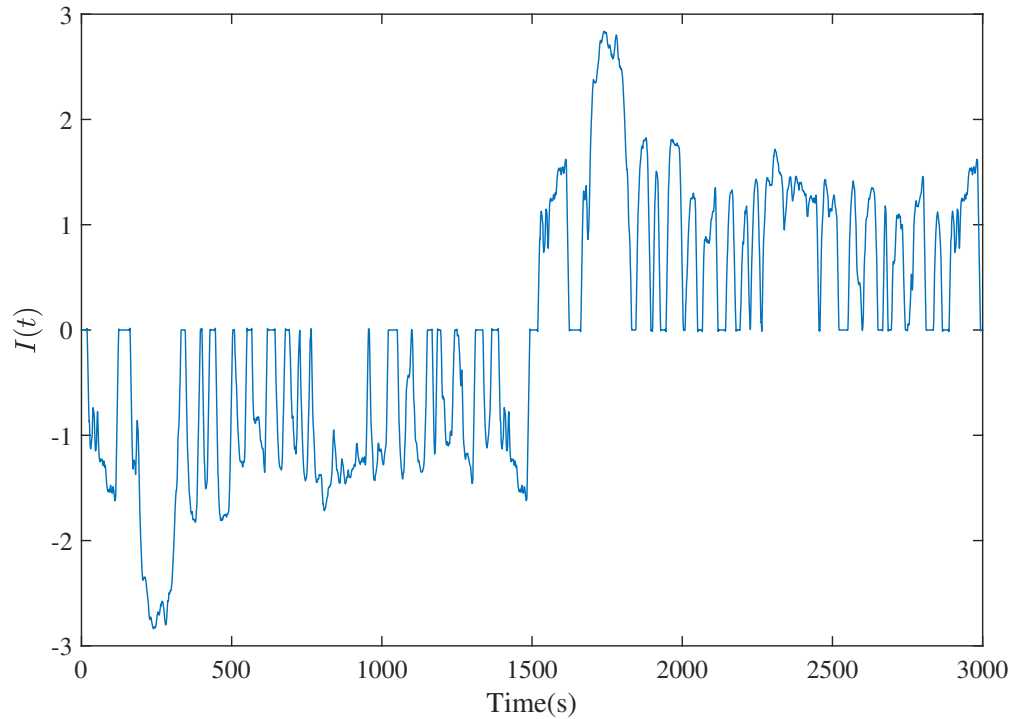
Figure 3.1: Modified UDDS Current Profile.

Table 3.3: SOC estimation error: EKF Simulation.

Test #	1	2	3	4	5	6	7	8
Root Mean Squared Error	0.096	0.66	0.12	0.037	0.16	0.87	0.09	0.403
Mean Absolute Error	4.8	12.3	0.23	0.062	4.51	13.6	0.30	0.427
Maximum Error	51.5	150	79.4	63.1	50.9	150	79.7	63.1

lations, the MAE does not exceed 14, and is typically below 5, with the exception of test settings #2 and #6. These two test settings have large process noise levels and low measurement noise levels. The ME for each simulation occurs within the first few time steps, as the EKF attempts to compensate for the initialization errors. The gain matrix, K, is high initially, which causes the estimated value to jump around at the beginning. The innovation, which is the difference between the estimated output and the measured output, also plays a role. At the beginning of the simulation, the initialization error is large, so the innovation is relatively large, and a large gain matrix K is obtained to correct the error. So fundamentally, the root cause of these large estimation errors can
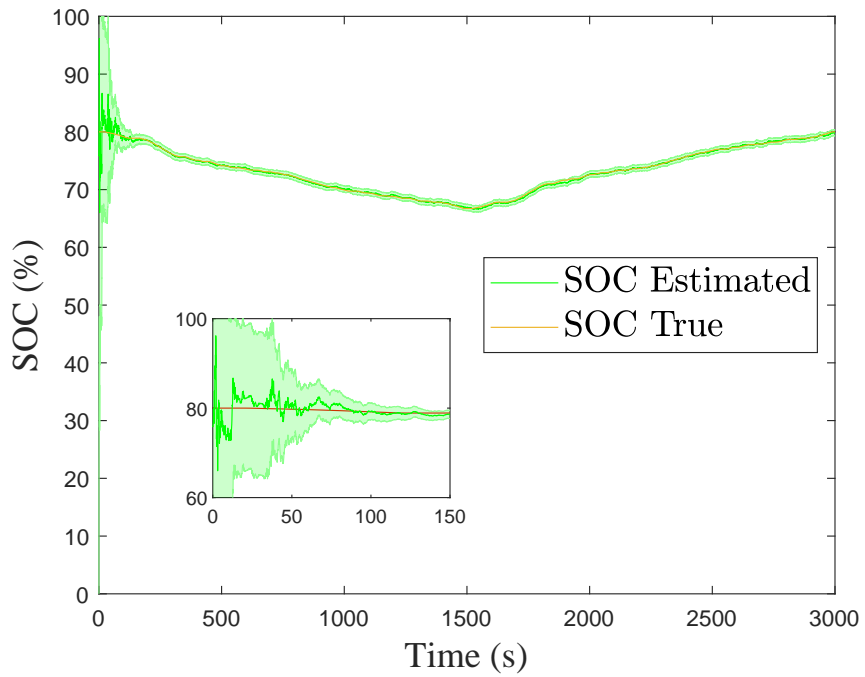
Figure 3.2: EKF-SOC estimation for simulation #3 in Table 3.2: Low initialization error with low process noise and high measurement noise.
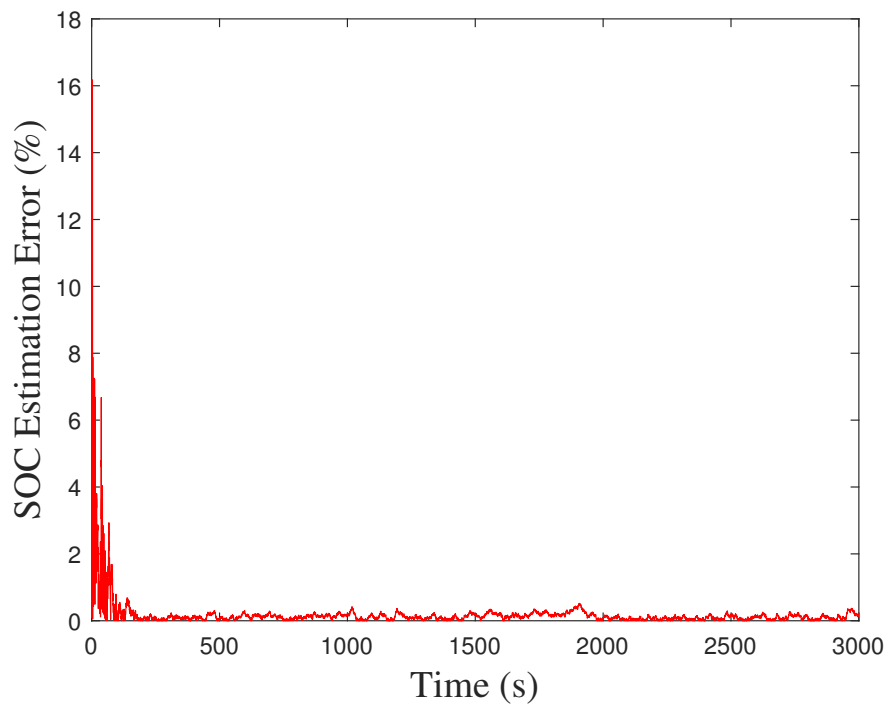
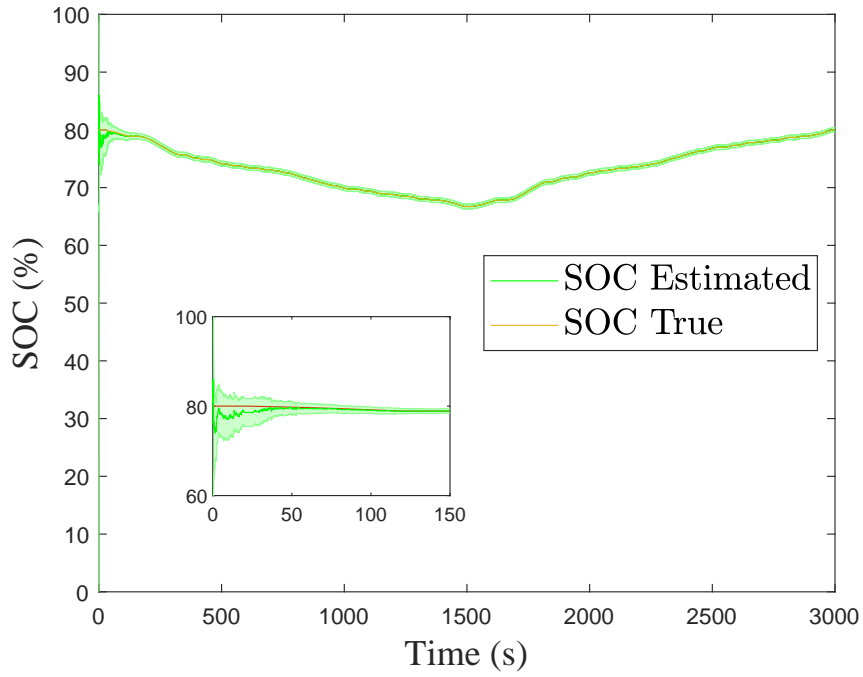Figure 3.3: SOC Estimation Error for simulation #3 in Table 3.2

Figure 3.4: EKF-SOC estimation for simulation #4 in Table 3.2: Low initialization error with low process noise and low measurement noise.
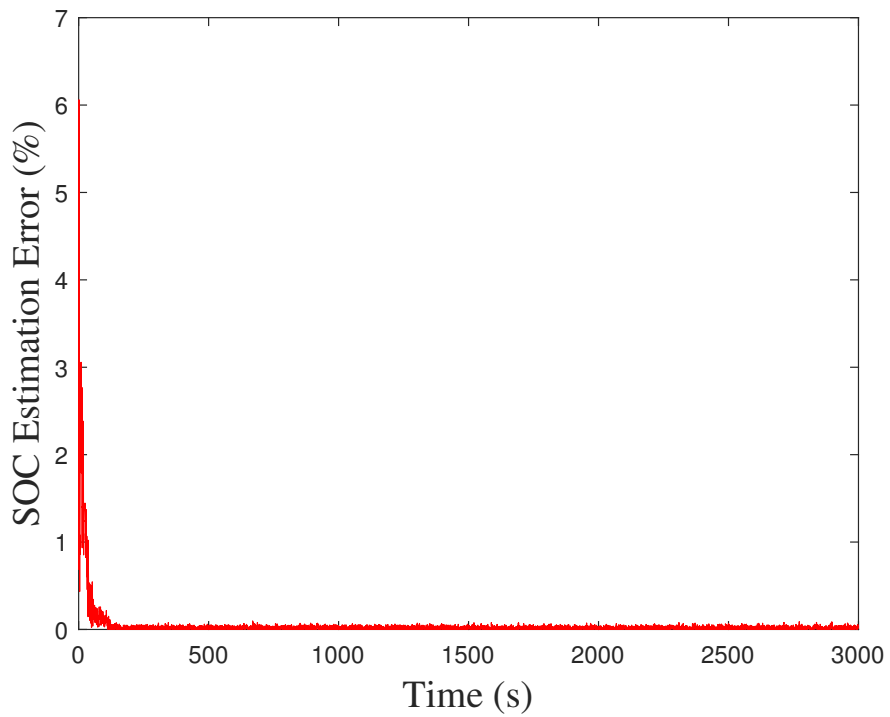

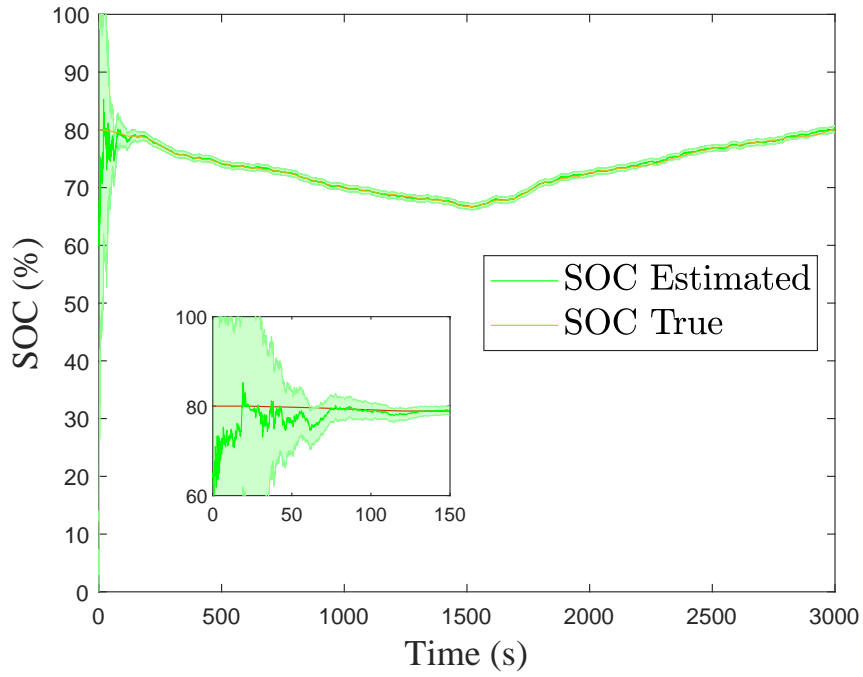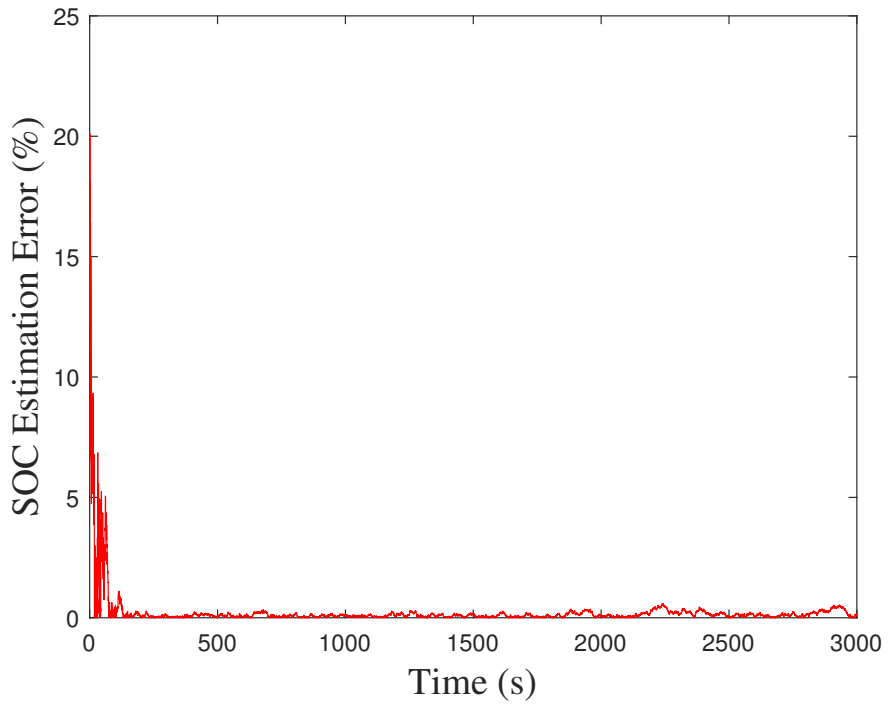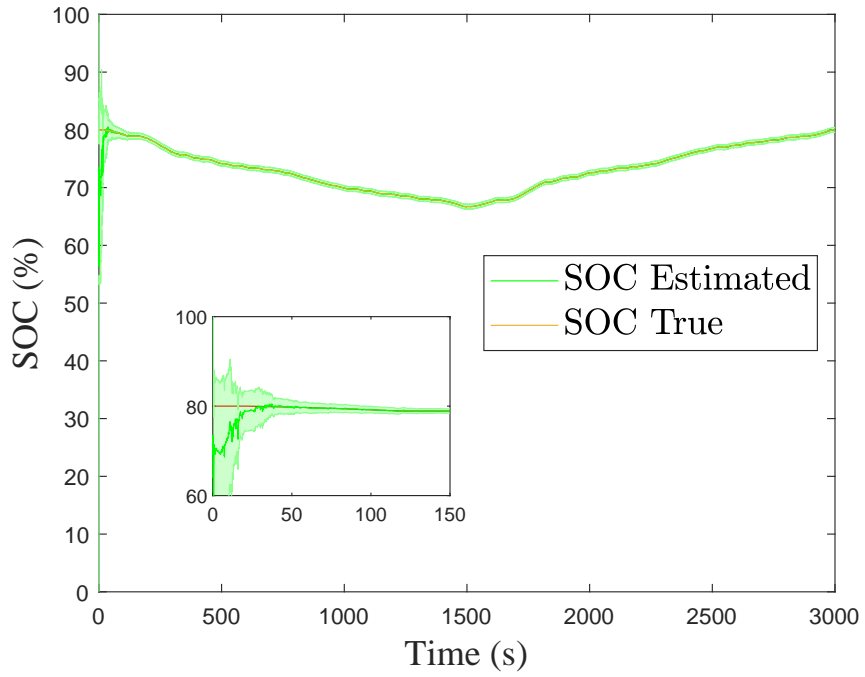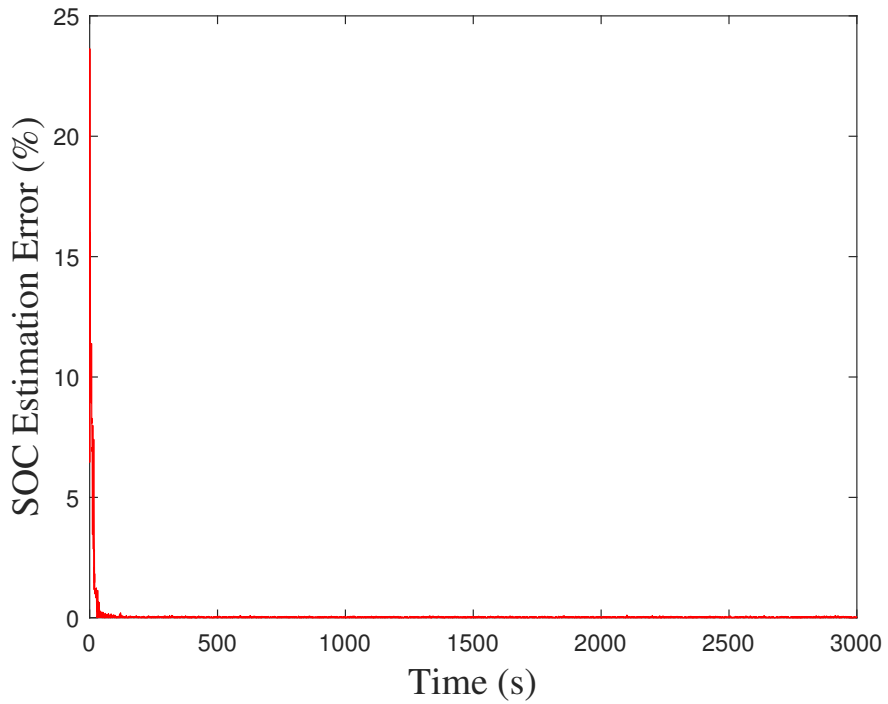Figure 3.5: SOC Estimation Error for simulation #4 in Table 3.2

32

Figure 3.6: EKF-SOC estimation for simulation #7 in Table 3.2: High initialization error with low process noise and high measurement noise.

Figure 3.7: SOC Estimation Error for simulation #7 in Table 3.2

33

Figure 3.8: EKF-SOC estimation for simulation #8 in Table 3.2: High initialization error with low process noise and low measurement noise.

Figure 3.9: SOC Estimation Error for simulation #8 in Table 3.2

be traced back to the initialization error.

3.3   Unscented Kalman Filter

Instead of approximating a nonlinear function, as is the case with the EKF, the UKF approximates the probability distribution of the system state. The state of the system is considered to be a Gaussian random variable. It is important to note that this probability distribution is assumed Gaussian, as it is analytically convenient for tracking the statistics of the Gaussian random variable. The UKF uses deterministic samples, known as sigma points, to track the statistics of the system state vector. These sigma points are able to characterize the first two moments of the state, the mean and the covariance. The UKF propagates the set of sigma points through the nonlinear system $f(x)$ and $g(x)$ given in Equation (3.1). According to [35], the UKF achieves second-order accuracy of the posterior mean and covariance estimates. Specifically, consider a nonlinear function $h(x)$, where x is a random variable — the unscented transform (UT), which is at the heart of the UKF, would compute the mean and covariance of $h(x)$ with second-order accuracy. In general, the UKF has been shown to perform better than the EKF, due to the approximation issues encountered in the EKF formulation. This is especially true for highly nonlinear systems, where the linearization employed by the EKF cannot accurately approximate the system at the estimate point.

To understand the UKF, one must first understand the UT. This method describes the process of calculating statistics of a nonlinearly transformed random variable. The idea is that a set of sample points, deterministically selected, can represent a random variable's distribution statistics, i.e., the mean and covariance. When the random variable is propagated through a nonlinear transformation, we can describe it by propagating the sample points through the nonlinear function to acquire a new set of sample points. These new sample points can describe the statistics of the nonlinearly transformed random variable.

The UT, in a general sense, is described here. Consider the random vector $x \in \mathbb{R}^n$ being passed through the nonlinear function $z = g(x)$, where the mean and covariance of random variable x are $\bar{x}$ and P^x, respectively. There will be $2n+1$ sigma points selected $\{x^i, i = 0, 1, ..., 2n\}$; the symmetry will be apparent in the equations below. Now that we have these preliminary definitions, we can

select the sigma points to represent the distribution as follows:

$$x^0 = \bar{x} \tag{3.9}$$

$$x^i = \bar{x} + \sqrt{n+\lambda}[\sqrt{P^x}]_i, \ i = 1, 2, ..., n \tag{3.10}$$

$$x^{i+n} = \bar{x} - \sqrt{n+\lambda}[\sqrt{P^x}]_i, \ i = 1, 2, ..., n \tag{3.11}$$

In these equations, λ is a scaling parameter described by the equation $\lambda = \alpha^2(n+\kappa) - n$ where α is usually a small positive number on the order of magnitude of 10^{-3} and κ is either 0 or $3 - n$. The notation $[]_i$ is used to represent the ith column of the matrix. The square root is defined in the Cholesky decomposition sense, $\sqrt{P^x}\sqrt{P^x}^T = P^x$. The sigma points are symmetrically spread about the mean, $\bar{x}$. When the sigma points are projected through the nonlinear function $g(\cdot)$, we obtain a new set of sigma points. The random variable z is transformed

$$z^i = g(x^i), \ i = 0, 1, 2, ...2n \tag{3.12}$$

We can then estimate the statistics of this transformed random variable as follows:

$$\bar{z} = E[g(x)] \approx \sum_{i=0}^{2n} W_i^m z^i \tag{3.13}$$

$$P^z = E[(g(x) - \bar{z})(g(x) - \bar{z})^T] \approx \sum_{i=0}^{2n} W_i^c (z^i - \bar{z})(z^i - \bar{z})^T \tag{3.14}$$

The weights are calculated using the following equations:

$$W_0^m = \frac{\lambda}{n+\lambda} \tag{3.15}$$

$$W_0^c = \frac{\lambda}{n+\lambda} + (1 - \alpha^2 + \beta) \tag{3.16}$$

$$W_i^m = W_i^c = \frac{1}{2(n+\lambda)}, \ i = 1, 2, ..., 2n \tag{3.17}$$

37

where β is equal to 2 if the distribution of x is Gaussian, which is the optimal setting. Now that the UT process has been laid out, we can proceed and apply these ideas to the KF problem. In the UKF, the UT will be used during the prediction and update steps.

Consider the general discrete-time nonlinear system given in Equation (3.1). Assume the mean and covariance of x_{k-1}, the state at time $k-1$, are given as $\hat{x}_{k-1|k-1}$ and $P^x_{k-1|k-1}$, respectively. The filter begins at the prediction step, where the algorithm seeks to generate sigma points for x_{k-1}.

State Prediction

$$\hat{x}^0_{k-1|k-1} = \hat{x}_{k-1|k-1} \tag{3.18}$$

$$\hat{x}^i_{k-1|k-1} = \hat{x}_{k-1|k-1} + \sqrt{n+\lambda} \left[\sqrt{P^x_{k-1|k-1}} \right]_i, \ i = 1, 2, ...n \tag{3.19}$$

$$\hat{x}^{i+n}_{k-1|k-1} = \hat{x}_{k-1|k-1} - \sqrt{n+\lambda} \left[\sqrt{P^x_{k-1|k-1}} \right]_i, \ i = 1, 2, ...n \tag{3.20}$$

Once the sigma points, $\{x^i_k, i = 0, 1, ..., 2n\}$, have been determined, they are passed through the nonlinear function of the process, $f(\cdot)$.

$$\hat{x}^{-,i}_{k|k-1} = f(\hat{x}^i_{k-1|k-1}), \ i = 0, 1, ..., 2n. \tag{3.21}$$

These nonlinearly transformed sigma points, $\hat{x}^{-,i}_{k|k-1}$, are used to characterize the mean and covariance of $f(x_{k-1})$, enabling the estimation of the priori x_k.

$$\hat{x}_{k|k-1} = E[f(x_{k-1})|Y_{k-1}] = \sum_{i=0}^{2n} W^m_i \hat{x}^{-,i}_{k|k-1} \tag{3.22}$$

$$P^x_{k|k-1} = E[(f(x_{k-1}) - \hat{x}_{k|k-1})(f(x_{k-1}) - \hat{x}_{k|k-1})^T |Y_{k-1}] + Q$$

$$= \sum_{i=0}^{2n} W^c_i (\hat{x}^{-,i}_{k|k-1} - \hat{x}_{k|k-1})(\hat{x}^{-,i}_{k|k-1} - \hat{x}_{k|k-1})^T + Q \tag{3.23}$$

where Y_{k-1} is the set of observations up to time $k-1$ and Q is the covariance of the additive process noise, w.

To proceed to the update step, the sigma points for the estimated state $\hat{x}_{k|k-1}$ at time k given information up to time $k-1$ must be computed.

State Update

$$\hat{x}_{k|k-1}^{+,0} = \hat{x}_{k|k-1} \tag{3.24}$$

$$\hat{x}_{k|k-1}^{+,i} = \hat{x}_{k|k-1} + \sqrt{n+\lambda}[\sqrt{P_{k|k-1}^x}]_i \ i = 1,2,....n \tag{3.25}$$

$$\hat{x}_{k|k-1}^{+,i+n} = \hat{x}_{k|k-1} - \sqrt{n+\lambda}[\sqrt{P_{k|k-1}^x}]_i \ i = 1,2,....n \tag{3.26}$$

After the sigma points for $x_{k|k-1}$ are computed, they are propagated through $h(\cdot)$ to find the sigma points for $h(x_k)$. These sigma points describe the predicted observation function:

$$\hat{y}_{k|k-1}^i = h(\hat{x}_{k|k-1}^{+,i}), i = 0,1,....,2n. \tag{3.27}$$

$$\hat{y}_{k|k-1} = E[y_k|Y_{k-1}] = \sum_{i=0}^{2n} W_i^m \hat{y}_{k|k-1}^i \tag{3.28}$$

$$P_{k|k-1}^y = E[(h(x_k) - \hat{y}_{k|k-1})(h(x_k) - \hat{y}_{k|k-1})^T|Y_{k-1}] + R$$
$$= \sum_{i=0}^{2n} W_i^c (\hat{y}_{k|k-1}^i - \hat{y}_{k|k-1})(\hat{y}_{k|k-1}^i - \hat{y}_{k|k-1})^T + R \tag{3.29}$$

$$P_{k|k-1}^{xy} = E[(x_k - \hat{x}_{k|k-1})(h(x_k) - \hat{y}_{k|k-1})^T|Y_{k-1}] = \sum_{i=0}^{2n} W_i^c (\hat{x}_{k|k-1}^i - \hat{x}_{k|k-1})(\hat{y}_{k|k-1}^i - \hat{y}_{k|k-1})^T \tag{3.30}$$

Using these statistics and parameters, the updated state estimate $\hat{x}_{k|k}$ and its covariance $P_{k|k}^x$ can be computed:

$$\hat{x}_{k|k} = \hat{x}_{k|k-1} + P_{k|k-1}^{xy}(P_{k|k-1}^y)^{-1}(y_k - \hat{y}_{k|k-1}) \tag{3.31}$$

$$P_{k|k}^x = P_{k|k-1}^x - P_{k|k-1}^{xy}(P_{k|k-1}^y)^{-1}(P_{k|k-1}^{xy})^T \tag{3.32}$$

3.3.1   UKF Simulation Results

In this section, simulation results are presented to validate the efficacy of the UKF applied to the NDC model to estimate the SOC of a battery, which is referred to as the NDC-UKF-SOC method. The NDC-UKF-SOC method was subjected to the same test settings as the NDC-EKF-SOC method, defined in Table 3.2, and the same transformed UDDS input current profile shown in Figure 3.1.

The UKF simulation results show that the NDC-UKF-SOC method has considerable robustness to different levels of initialization errors and noise. This robustness will make the method advantageous in real-world applications, along with the low computational complexity of the algorithm. The UKF simulation errors are summarized in Table 3.4, and four cases are plotted in Figures 3.10, 3.12, 3.14, and 3.16, along with their respective estimation error plots.

The same cases are shown for the UKF as with the EKF: low process noise and both modes, high and low, of initialization error and measurement noise. In Figure 3.10, the NDC-UKF-SOC method is shown to converge roughly 75 seconds into the simulation, as can be seen in the zoomed-in snapshot at the top of the figure. The true SOC value is within the shaded (2-σ) region of the estimated SOC throughout the majority of the simulation. The true SOC is outside of this confidence region around 2,100 seconds, but regains entry around 2,200 seconds. The confidence region grows smaller over time, which is a reflection of the estimation covariance matrix — theoretically, this matrix should decrease in magnitude as the filter progresses and receives new measurements. The shaded confidence region shrinks relatively quickly, around 30 seconds into the simulation, in Figure 3.12. This test setting has low measurement noise, which may play a role in the faster rate of decrease of the estimation covariance matrix. The true SOC falls outside of the confidence region a few times during this simulation, but never strays too far and overall shows a low estimation error. With an initialization error of 20%, the NDC-UKF-SOC method converges around 250 seconds, about 4 minutes, into the simulation, shown in Figure 3.14. After the estimation converges, the true SOC value remains within the 2-σ region of the estimated SOC for most of the simulation, and a consistently low error is reported in Figure 3.15. In Figure 3.16, the NDC-UKF-SOC method

40

Table 3.4: SOC estimation error: UKF Simulation.

Test #	1	2	3	4	5	6	7	8
Root Mean Squared Error	1.89	3.06	0.16	0.52	0.22	5.6	0.19	0.39
Mean Absolute Error	5.27	7.19	0.47	0.69	5.68	10.5	0.67	0.67
Maximum Error	39.9	159	80.3	66.6	80.5	54.8	80.8	64.4

shows a similar convergence time as in test setting #7, after compensating for the 20% initialization error. The true SOC value dips below the 2-σ region of the estimated SOC around 1,500 seconds and regains confidence around the inflection point at 1,700 seconds, then dips below again around 2,200 seconds and once again enters the confidence region around 2,500 seconds.
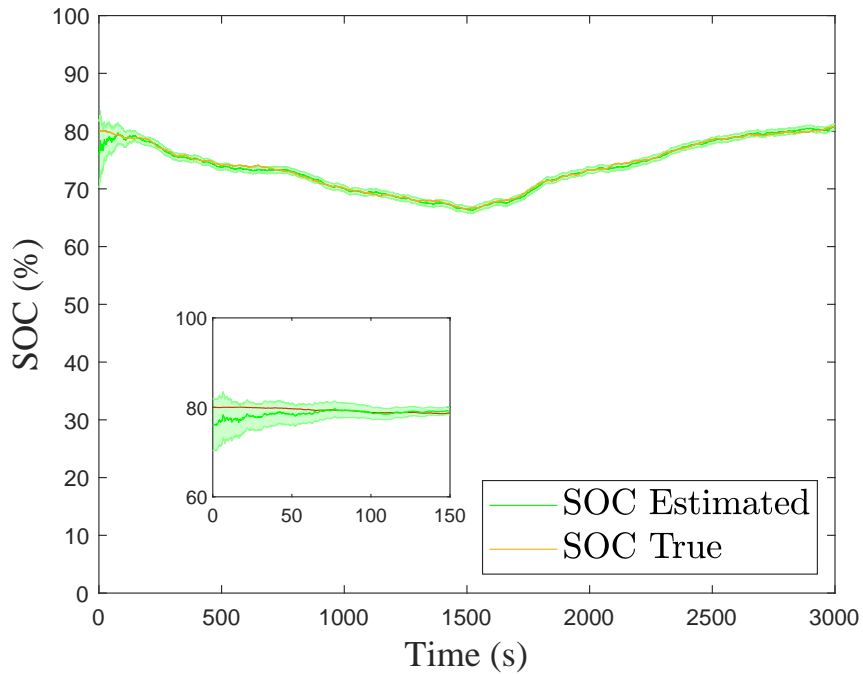
Figure 3.10: UKF-SOC estimation for simulation #3 in Table 3.2: High initialization error with low process noise and low measurement noise.

The SOC estimation error for the UKF simulations is shown in Table 3.4. Three error metrics are reported: RMSE, MAE, and ME. The RMSE values are low in all cases, except for test #2 and #6. These cases, with high process noise levels and low measurement noise levels, show the largest
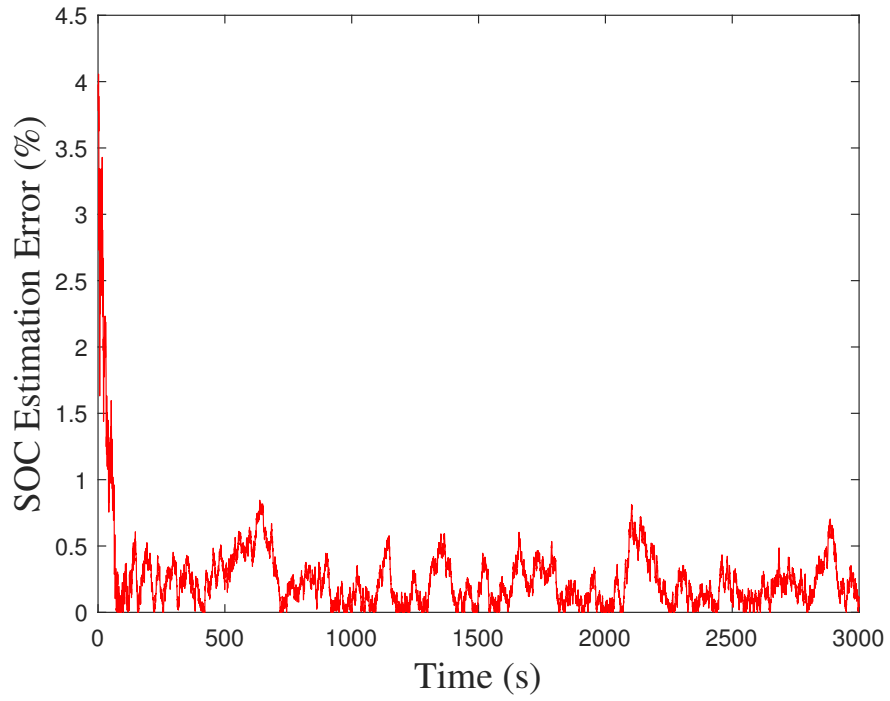
Figure 3.11: UKF-SOC estimation error for simulation #3 in Table 3.2.
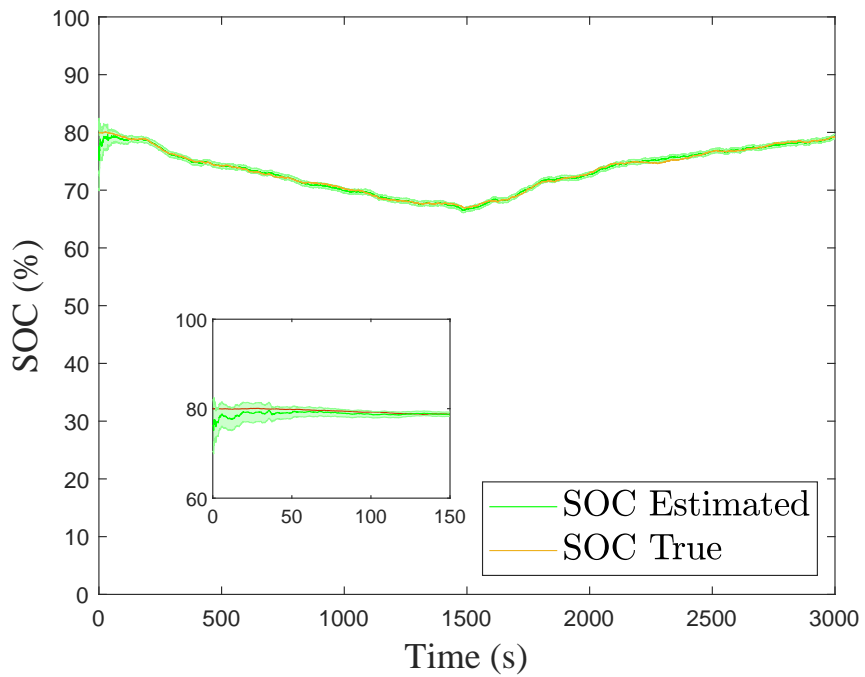
Figure 3.12: UKF-SOC estimation for simulation #4 in Table 3.2: High initialization error with low process noise and low measurement noise.
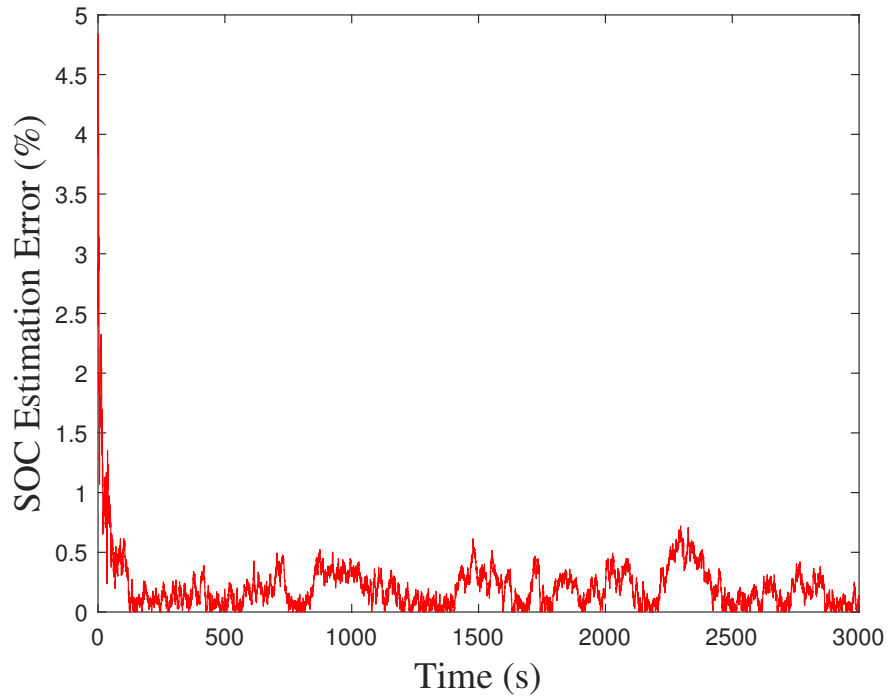
42

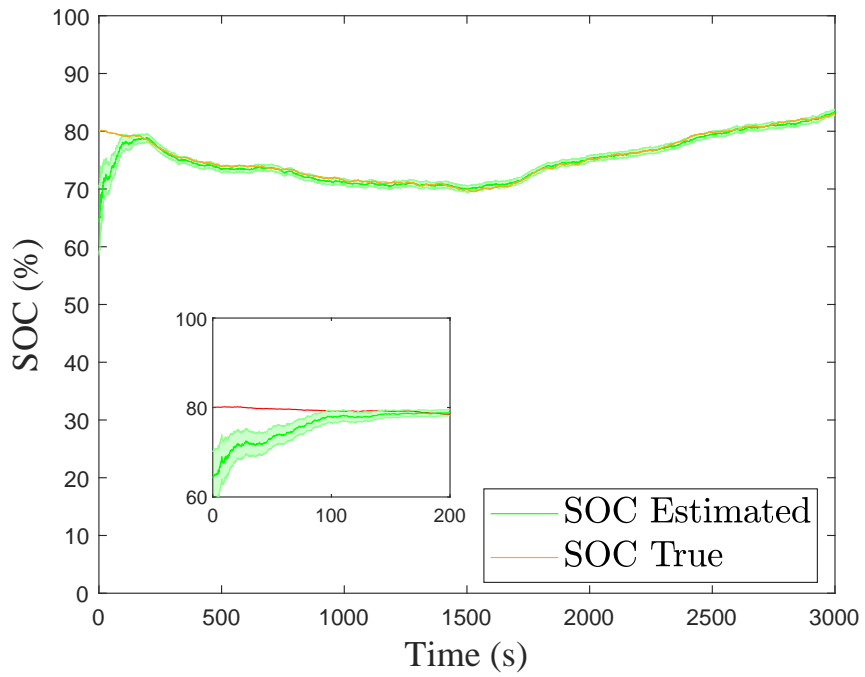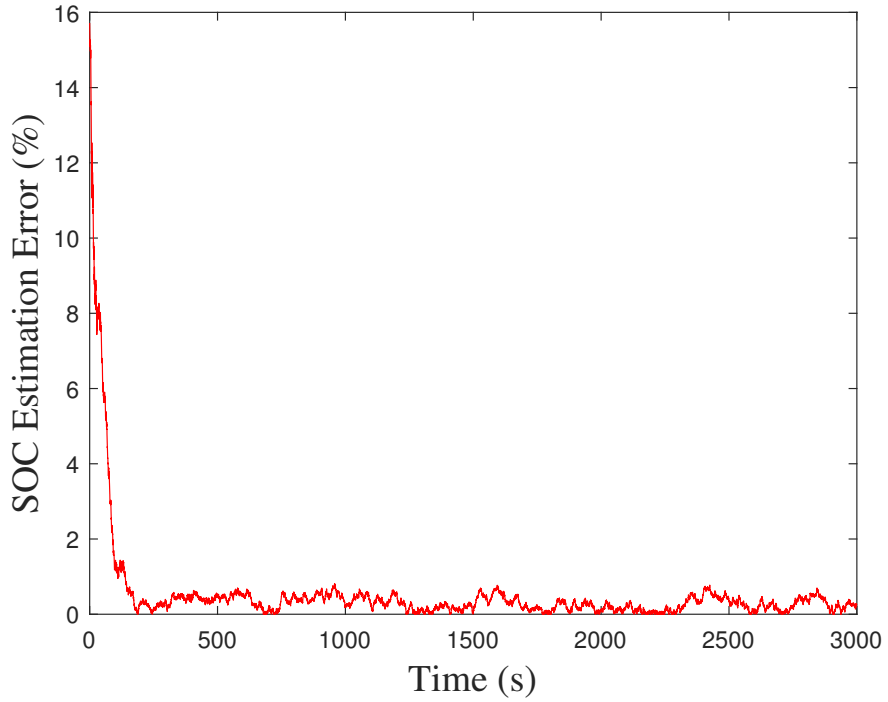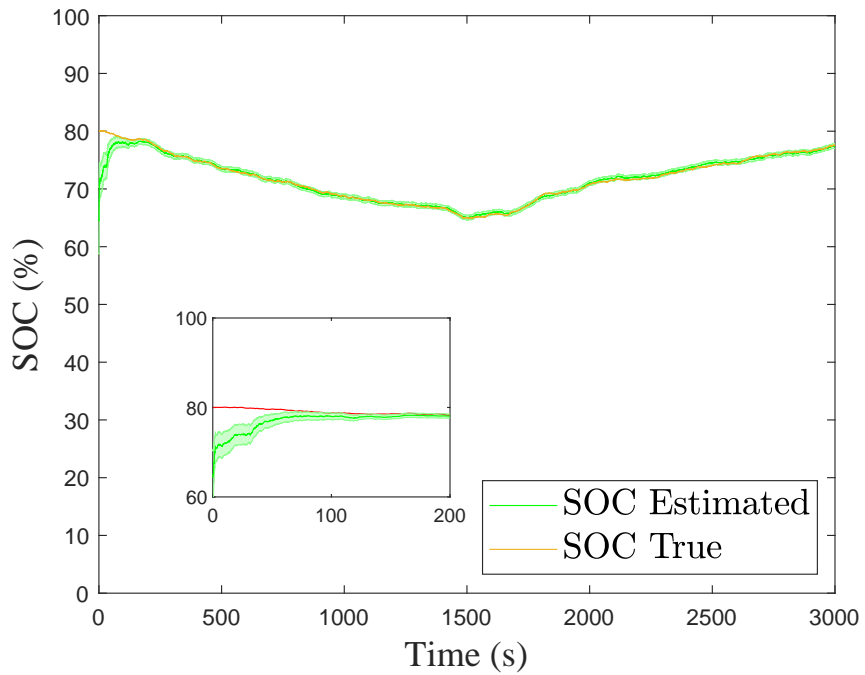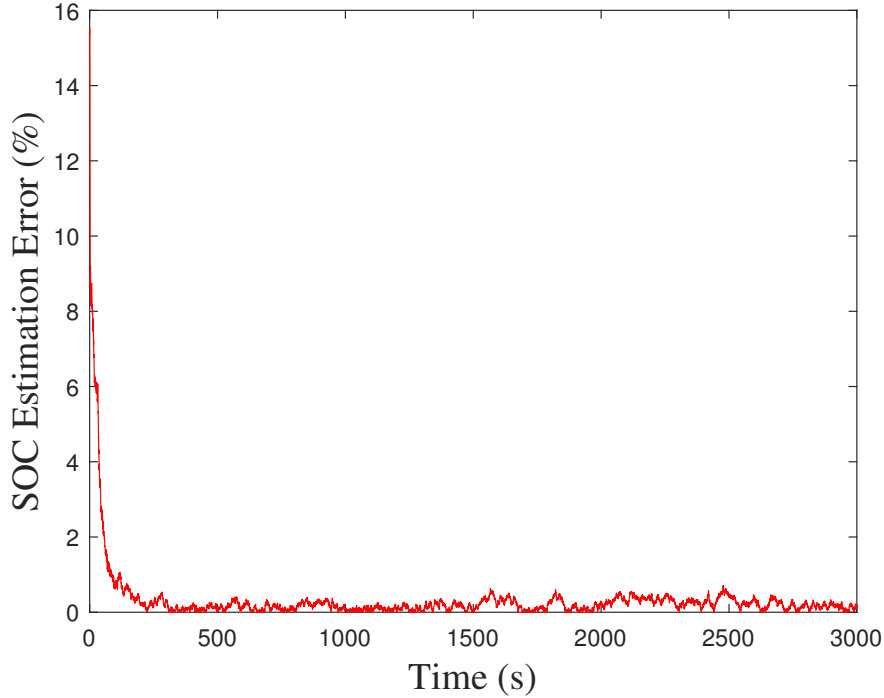Figure 3.13: UKF-SOC estimation error for simulation #4 in Table 3.2.

Figure 3.14: UKF-SOC estimation for simulation #7 in Table 3.2: High initialization error with low process noise and high measurement noise.

Figure 3.15: UKF-SOC estimation error for simulation #7 in Table 3.2.

Figure 3.16: UKF-SOC estimation for simulation #8 in Table 3.2: High initialization error with low process noise and low measurement noise.

Figure 3.17: UKF-SOC estimation error for simulation #8 in Table 3.2.

errors. However, the MAE reported for these tests are 7.19 and 10.5 respectively, which are lower than that of the EKF for these test cases. This seems to suggest that a low measurement noise may not always be beneficial — in this case it performs worse than test settings #1 and #5 which have high process noise levels as well as high measurement noise. Throughout all UKF simulations, the MAE is typically around or below 5%, with the exception of test settings #2 and #6. The ME for each simulation occurs within the first few time steps, as the UKF attempts to compensate for the initialization errors. The large ME values may be attributed to the large initialization error, as the largest errors usually occur at the beginning of the simulation.

3.4   Chapter Summary

In this chapter, extensive simulation was carried out for the NDC model, using both an EKF and UKF in a variety of test cases. This chapter introduced the EKF and UKF approaches for state estimation, investigated their application to SOC estimation based on the NDC model, and presented extensive simulation results in a variety of test cases. Typically, the EKF showed similar conver-

gence times to the UKF. For both estimation methods, NDC-EKF-SOC and NDC-UKF-SOC, the SOC estimation was very accurate and the error shading showed that as time progressed, the algorithms became more accurate and precise. For the most part, the true SOC lied within the 2-σ (95.45%) confidence bound. In the next chapter, these methods will be verified via experimental data.

Chapter 4

Experimental Validation

4.1 Test Design and Setup

The battery testing presented in this work was conducted on a PEC® SBT4050 battery tester, shown in Figure 4.1. The battery tester is capable of up to 40 V and 50 A charging and discharging, and can be programmed for specific test regimes and profiles. These testing profiles, also called scripts, can be formulated offline, and are stored and called on the server. The software used to write the test scripts is called LifeTest®. The scripts, organized in step format, can be time- or event-driven. The software can perform basic, pre-programmed charging and discharging procedures, such as constant-current constant-voltage, as well as user-defined tests, such as a UDDS profile. The data was collected using the LifeTest® software, and included delta time, current, and cell voltage. The sampling rate of the battery tester is 1000 Hz and it collects the data using 4-point measurement and differential input. The experiments were performed on a Panasonic NCR18650B lithium-ion battery cell, which has a nominal voltage of 3.7 V and a capacity of 3.07 Ah. The discharging current was scaled to a maximum of 3 A, which is a 1 C-rate discharge — this means the battery will fully discharge from a full charge in 1 hour at 3 A. The cell is considered fully discharged at 3.2 V, and fully charged at 4.2 V.

The RC parameter set used in these experiments, which is unique to the Panasonic NCR18650B LiB and obtained in [1], is shown in Table 4.1 and the SOC-OCV parameters are shown in Equation (4.1).

$$\alpha = \begin{bmatrix} 3.16 & 2.72 & -8.33 & 15.12 & -12.17 & 3.61 \end{bmatrix} \tag{4.1}$$

Table 4.1: NDC model parameters.

C_b	C_s	R_b	R_s	R_1	C_1
10037	973	0.019	0	0.02	3250
[F]	[F]	[Ω]	[Ω]	[Ω]	[F]

The function $h(\cdot)$ is now defined, and we have an explicit relationship between SOC and OCV:

$$\text{OCV} = h(\text{SOC}) = 3.16 + 2.72 \cdot \text{SOC} - 8.33 \cdot \text{SOC}^2 + 15.12 \cdot \text{SOC}^3 - 12.17 \cdot \text{SOC}^4 + 3.61 \cdot \text{SOC}^5$$
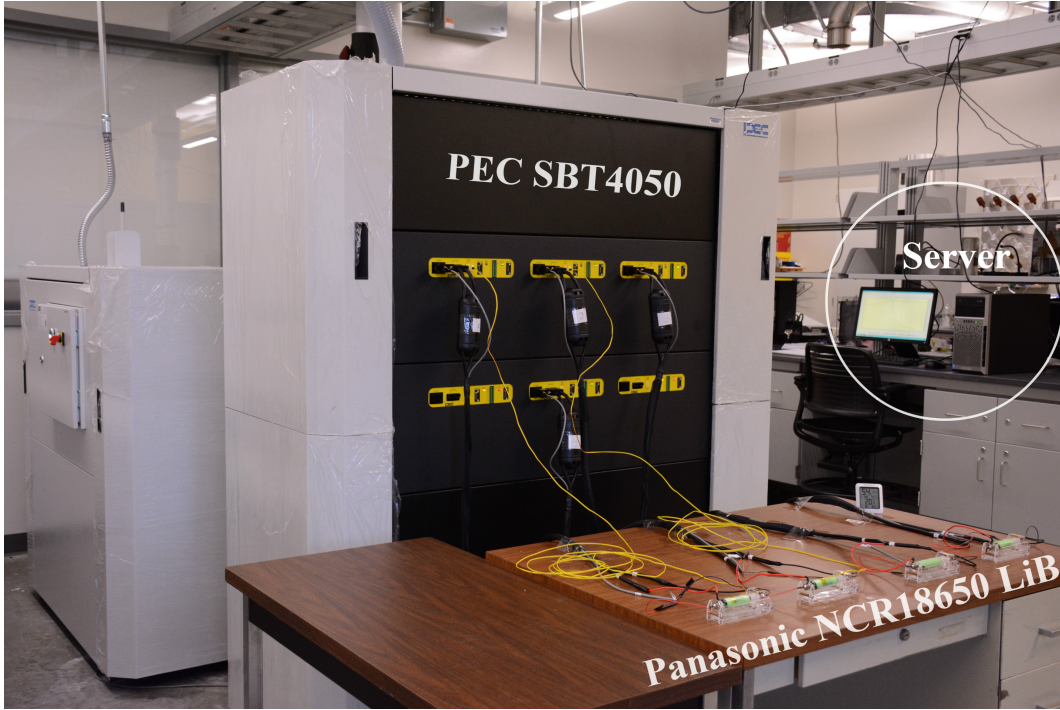
(4.2)

Figure 4.1: PEC® SBT4050 battery cycler test bench set-up from [1].

For the experimental validation, the estimation accuracy is analyzed under different initialization errors. Unlike in the simulation setting, we cannot change the measurement noise levels — the sensors in the PEC tester will experience a certain noise level depending on the signal noise from the ambient environment, the wires connecting the sensors to the data acquisition board, and the circuitry in the sensors themselves. Even though this noise level is unknown at first, one can tune the Q and R matrices in the EKF and UKF accordingly to capture the presence of measurement

Table 4.2: Experiment test design.

Test #	1	2	3	4
Initialization Error (%)	5	20	50	75

noises and improve the estimation performance. It is common in practice to use ad hoc method-ologies, such as trial and error, to discover the optimal value of the system noise. The input current amperage and measured terminal voltage, shown in Figures 4.2 and 4.3, were used to verify the proposed SOC estimation algorithms — NDC-EKF-SOC and NDC-UKF-SOC. The input current is normalized from the UDDS profile [34] and scaled to a discharging range of 0–3 A. Similar to the simulation testing design, the experimental test cases can be seen in Table 4.2. In the experi-mental setting, SOC obtained by coulomb counting is used as a reference to evaluate the estimation by the NDC-EKF-SOC and NDC-UKF-SOC algorithms [36].
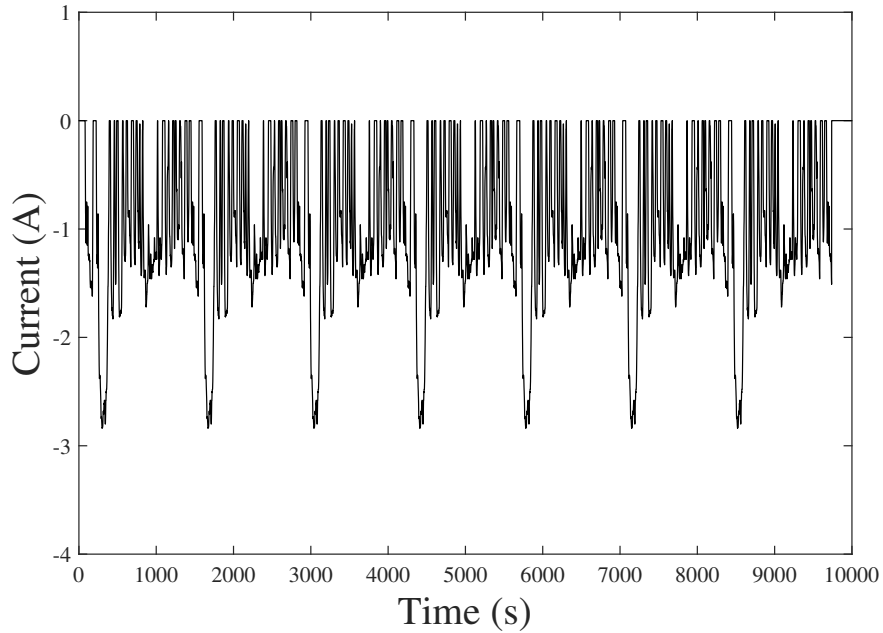
Figure 4.2: UDDS-based current profile.
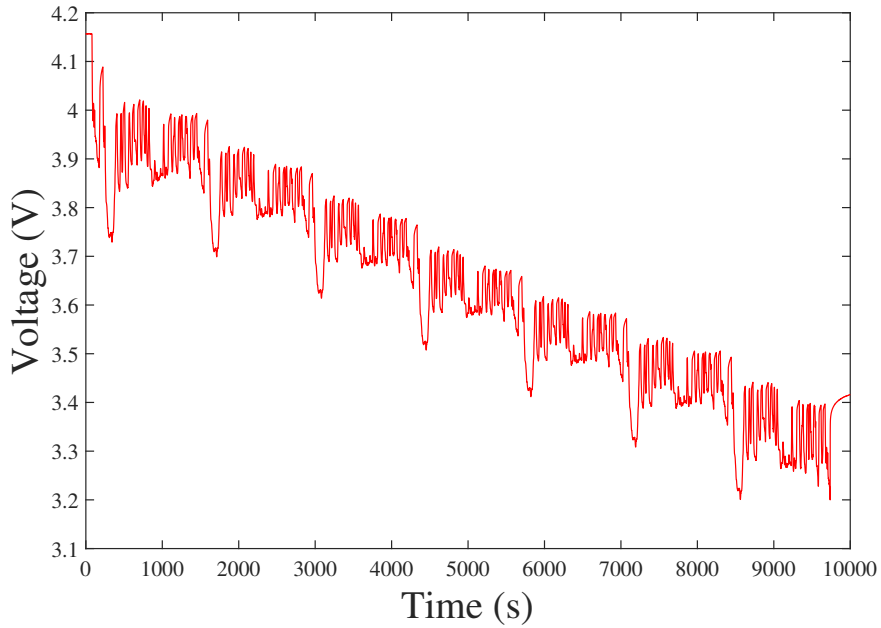
Figure 4.3: measured terminal voltage.

4.2 EKF Results

Using the experimental data, the EKF was able to track the SOC of the battery very well, with an average RMSE of 1.58 across all four experimental settings, as reported in Table 4.3. The MAE was also quite low, with an average of 1.81 across all experimental settings. The ME for the EKF was capped by the initialization error in test settings #2, #3, and #4. In test setting #1, the ME slightly surpassed the initial error of 5% to reach 6.16.

The EKF experimental results are shown in the following figures. The SOC estimation for test setting #1 is shown in Figure 4.4 and the corresponding error is plotted in Figure 4.5. Each experimental case is plotted thereafter. Overall, the EKF method shows accurate SOC tracking under high initialization error, even up to 75%.

Table 4.3: SOC estimation error EKF: Experimental data.

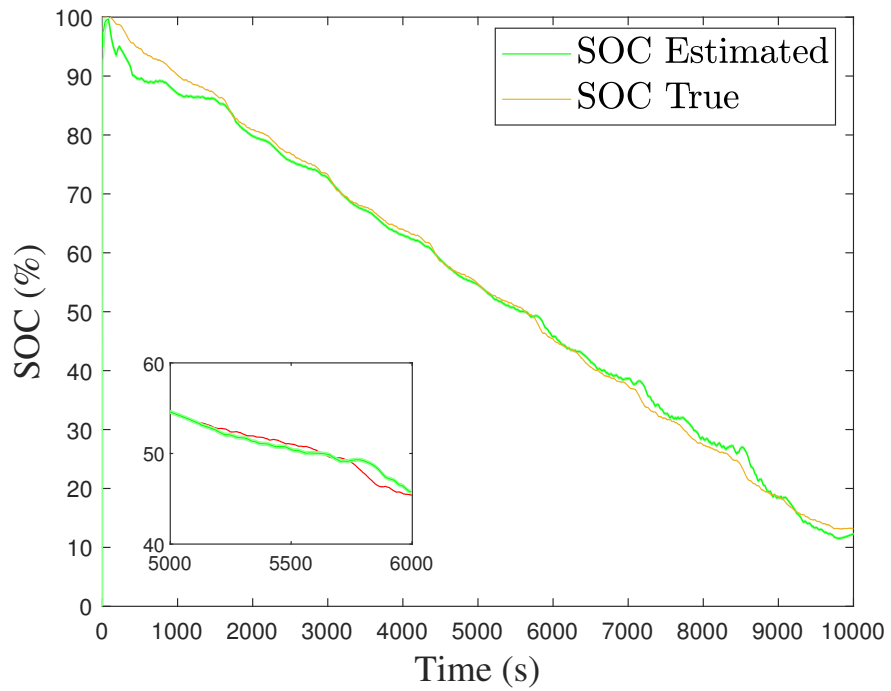| Test #	1	2	3	4
Root Mean Squared Error (% SOC)	1.19	2.41	1.51	1.19
Mean Absolute Error (% SOC)	1.53	2.43	1.77	1.51
Maximum Error (% SOC)	6.16	20	50	75

50

Figure 4.4: EKF-SOC estimation based on the experimental data using the test setting #1 in Table 4.2.
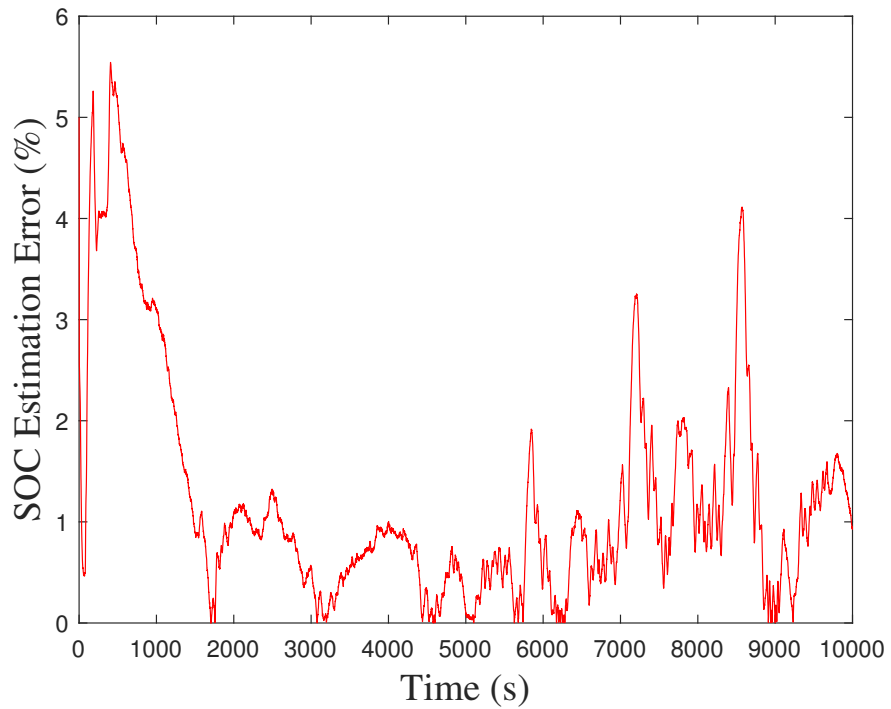

Figure 4.5: EKF-SOC estimation error for experimental setting #1 in Table 4.2.
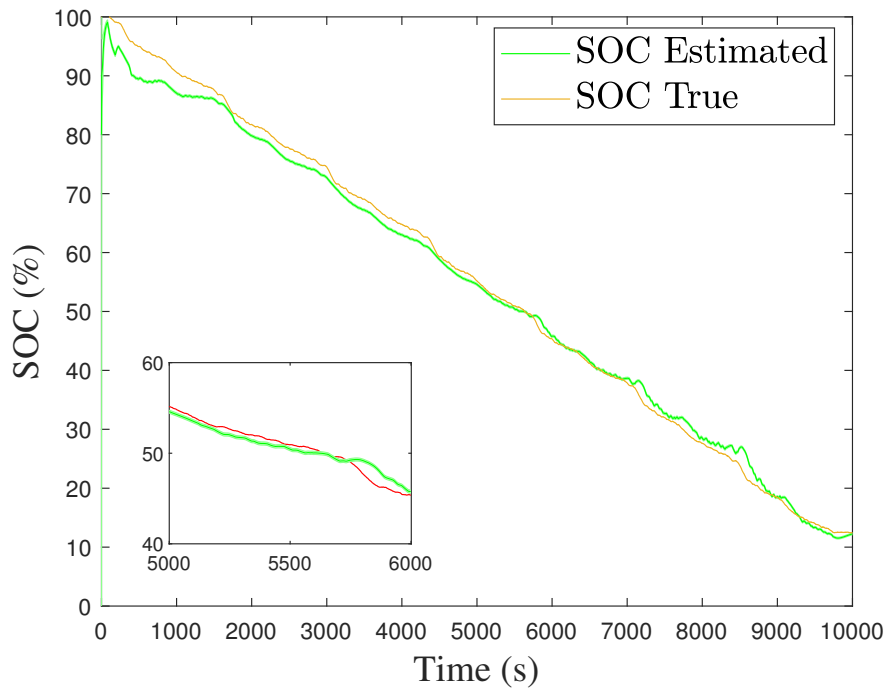
Figure 4.6: EKF-SOC estimation based on the experimental data using the test setting #2 in Table 4.2.
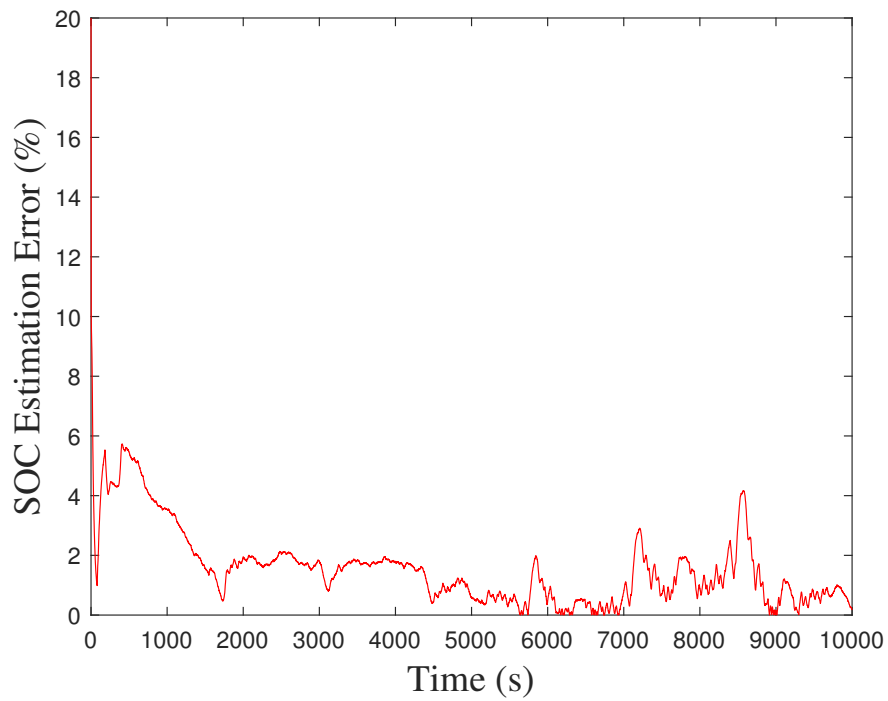

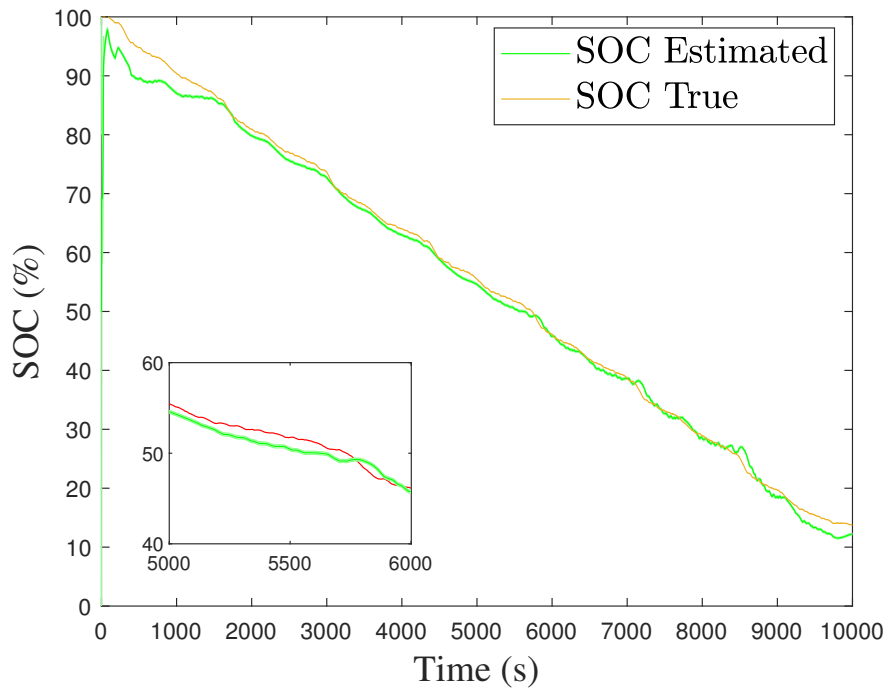Figure 4.7: EKF-SOC estimation error for experimental setting #2 in Table 4.2.

Figure 4.8: EKF-SOC estimation based on the experimental data using the test setting #3 in Table 4.2.
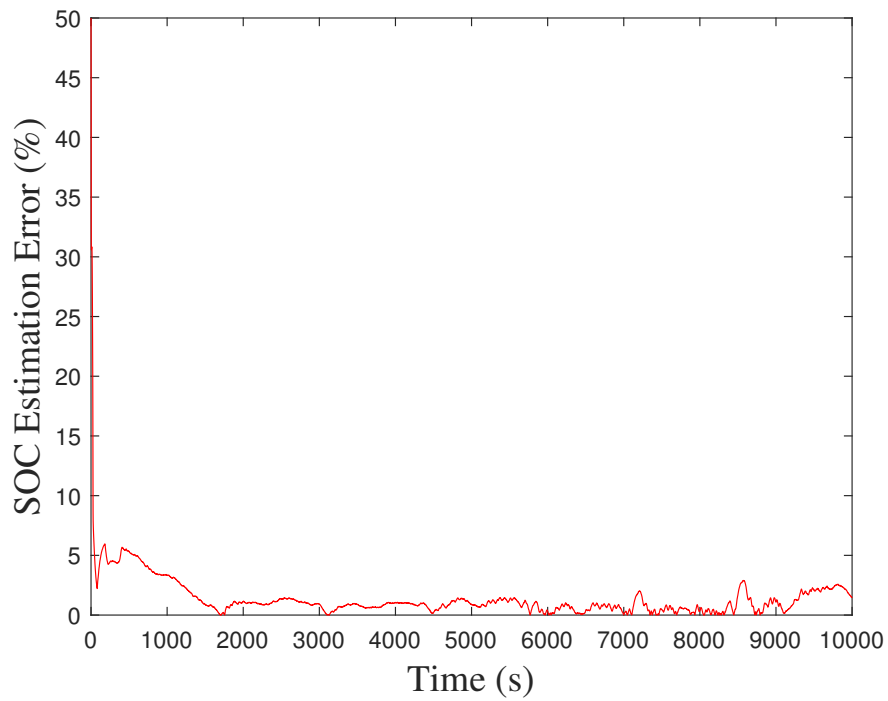

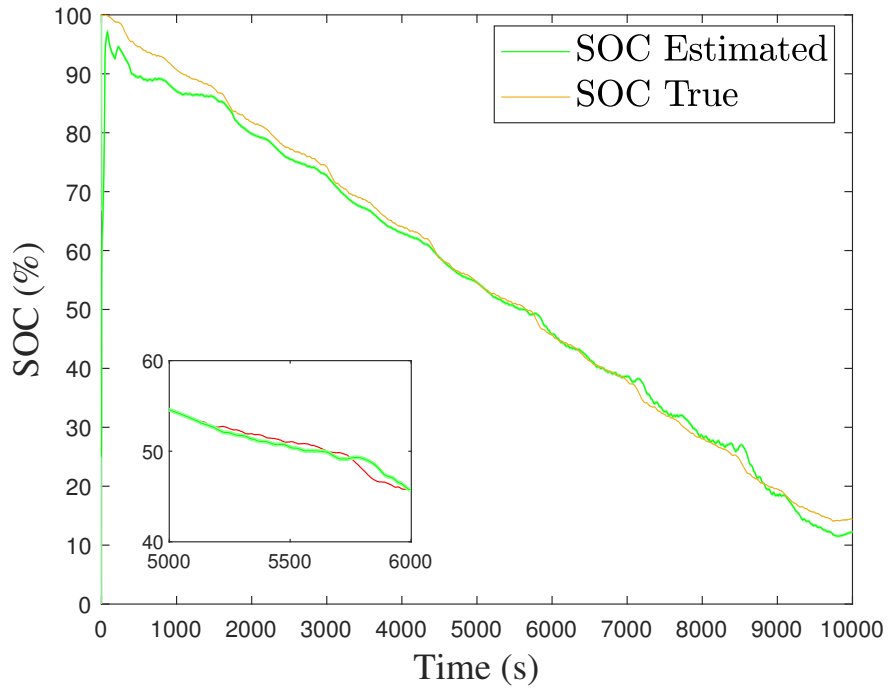Figure 4.9: EKF-SOC estimation error for experimental setting #3 in Table 4.2.

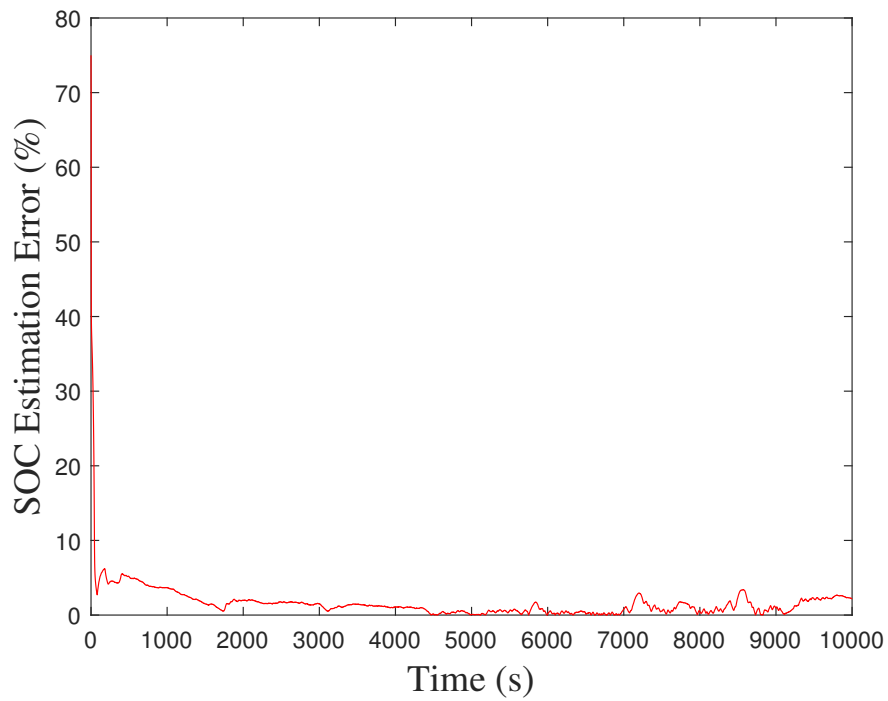Figure 4.10: EKF-SOC estimation based on the experimental data using the test setting #4 in Table 4.2.

Figure 4.11: EKF-SOC estimation error for experimental setting #4 in Table 4.2.

4.3   UKF Results

In this section, the UKF method is shown to be verified by experimental results. The UKF algorithm was verified using the same input-output data, i.e., input UDDS current and measured terminal voltage, as previously mentioned in the EKF experimental results section. The UKF was able to track the SOC of the battery to a higher accuracy than that of the EKF method, with an average RMSE of 0.077 across all four experimental settings, as reported in Table 4.3. The MAE was also lower than that of the EKF method, with an average of 0.81 across all experimental settings. The ME for the UKF was capped by the initialization error in test settings #2, #3, and #4. In test setting #1, the ME slightly surpassed the initial error of 5% to reach 7.3.

The UKF experimental results are shown in the following figures. The SOC estimation for test setting #1 is shown in Figure 4.12 and the corresponding error is plotted in 4.13. Each experimental case is plotted thereafter. Overall, the UKF method shows very accurate and convergent SOC tracking under high initialization error, even up to 75%, and is the better option when compared with the EKF in the experimental setting.
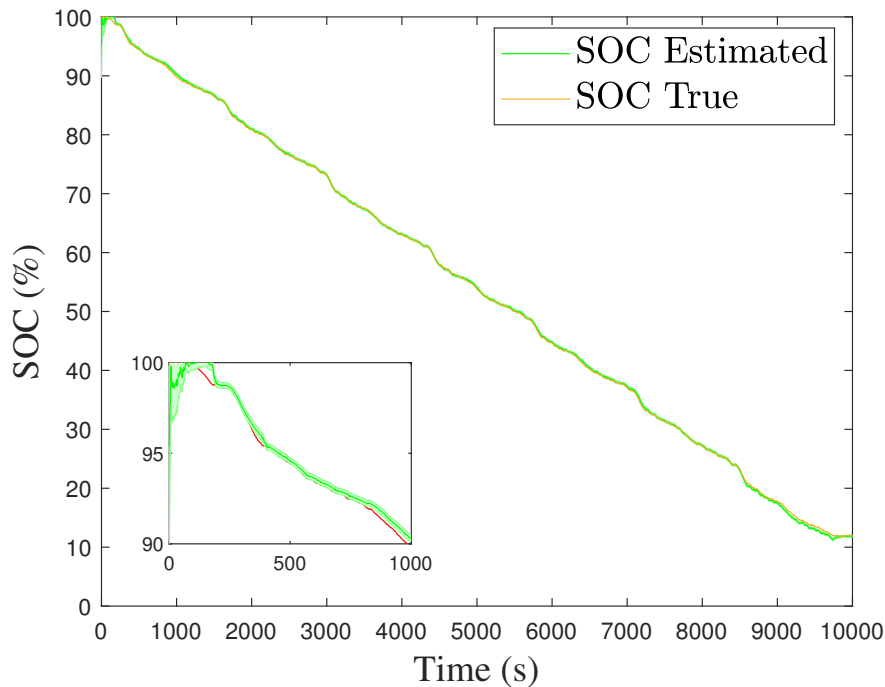

Figure 4.12: UKF-SOC estimation based on the experimental data using the test setting #1 in Table 4.2.
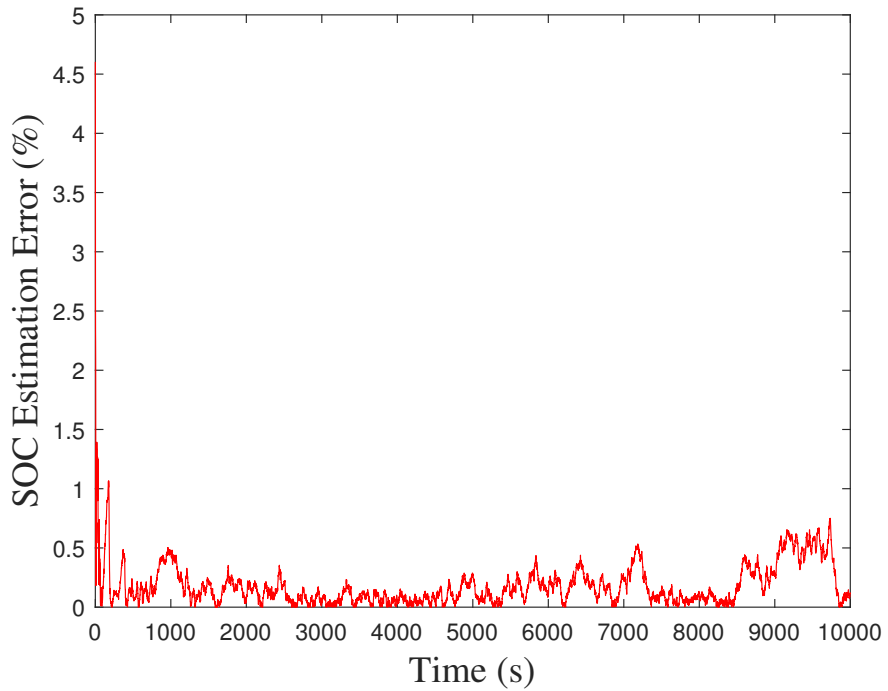
Figure 4.13: UKF-SOC estimation error for experimental setting #1 in Table 4.2.

Figure 4.14: UKF-SOC estimation based on the experimental data using the test setting #2 in Table 4.2.

Figure 4.15: UKF-SOC estimation error for experimental setting #2 in Table 4.2.
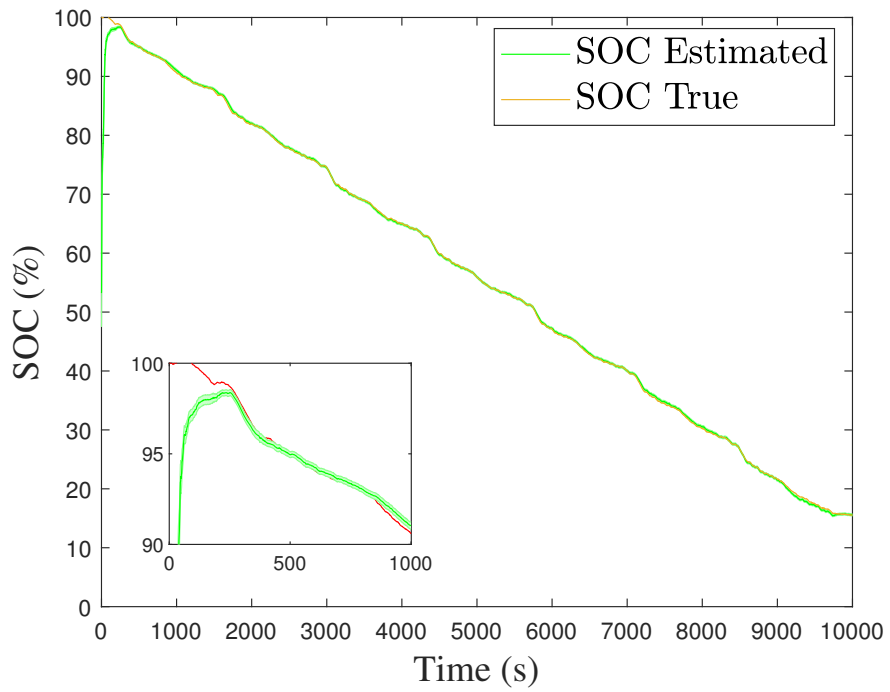
Figure 4.16: UKF-SOC estimation based on the experimental data using the test setting #3 in Table 4.2.

Figure 4.17: UKF-SOC estimation error for experimental setting #3 in Table 4.2.
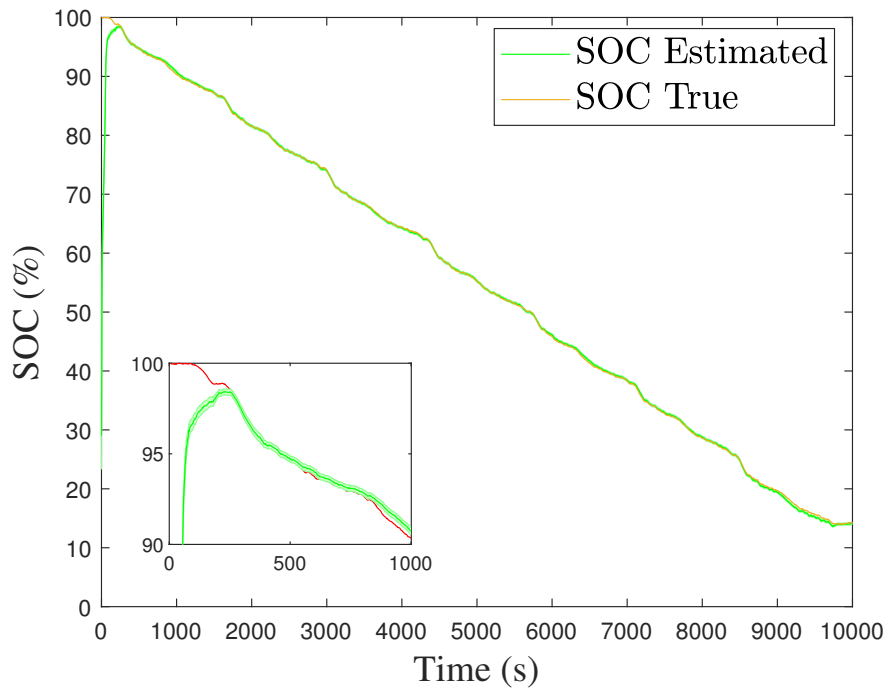
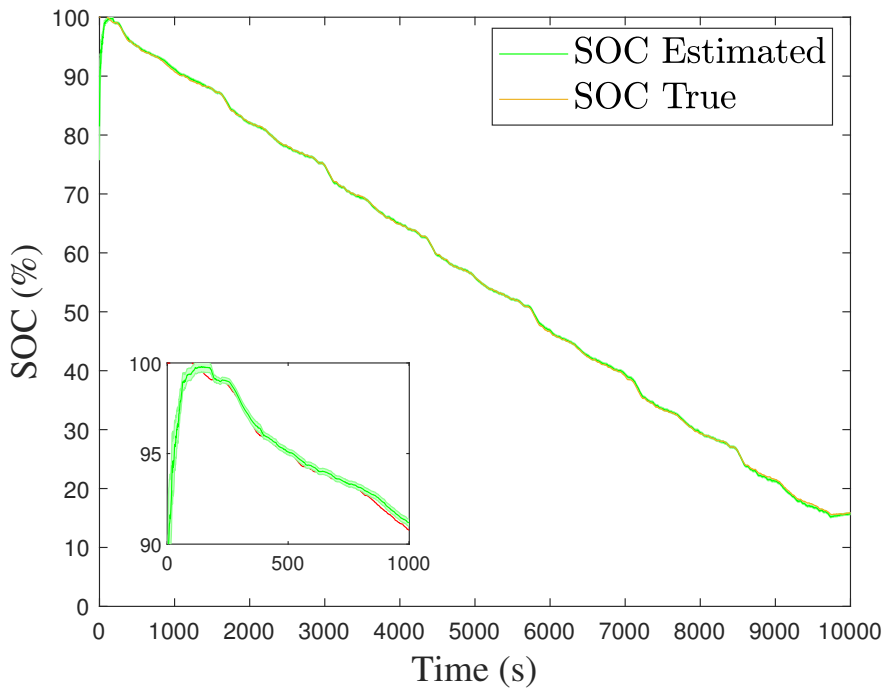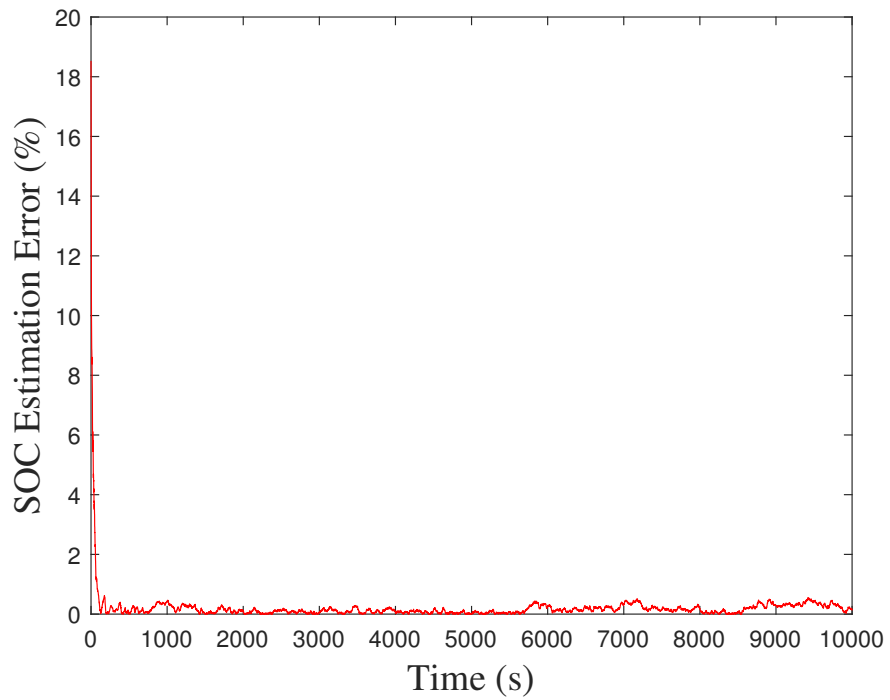

Figure 4.18: UKF-SOC estimation based on the experimental data using the test setting #4 in Table 4.2.
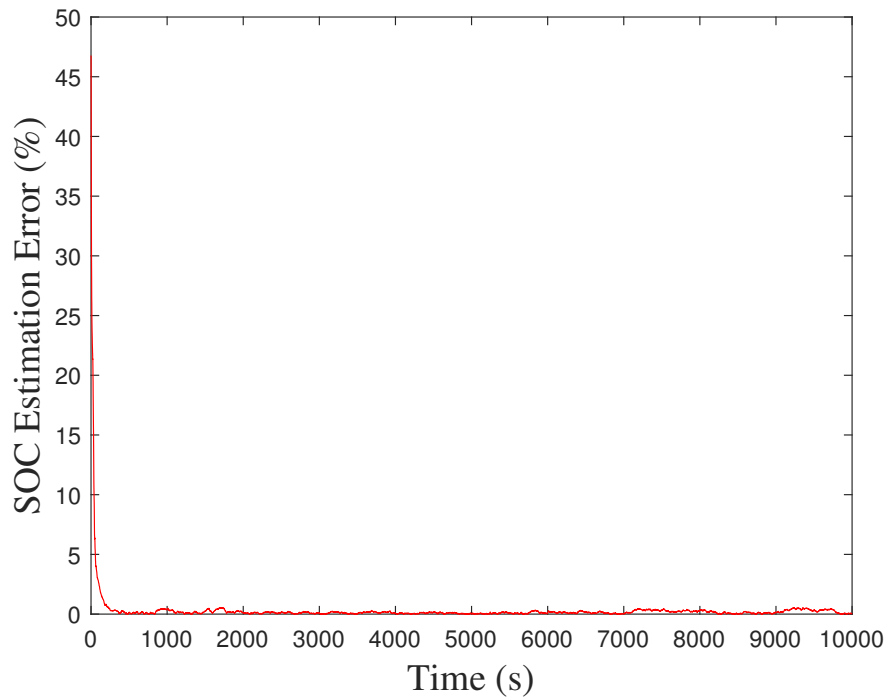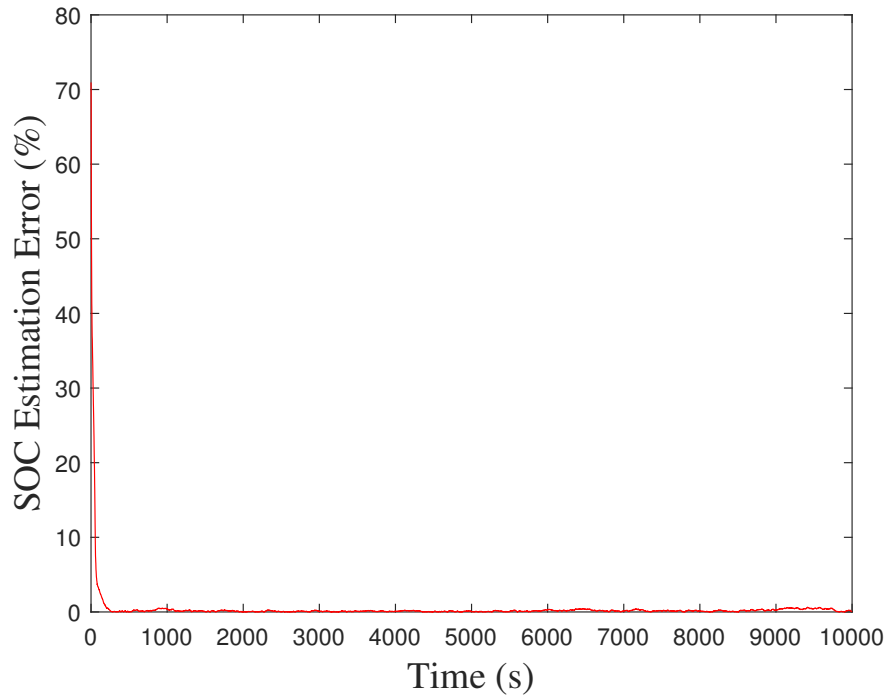
Figure 4.19: UKF-SOC estimation error for experimental setting #4 in Table 4.2.

Table 4.4: SOC estimation error UKF: Experimental data.

Test #	1	2	3	4
Root Mean Squared Error (% SOC)	0.03	0.0006	0.096	0.18
Mean Absolute Error (% SOC)	0.18	0.22	0.31	0.39
Maximum Error (% SOC)	7.3	18.6	46.8	71

4.4 Chapter Summary

In this section, the NDC model was tested using data obtained through experiments done on a Panasonic NCR18650B LiB cell. The NDC-UKF-SOC algorithm was able to track the reference SOC with higher accuracy than the NDC-EKF-SOC algorithm. This is to be expected as the UKF has a higher order of accuracy, theoretically speaking, than the EKF. Even though the NDC-UKF-SOC outperformed the NDC-EKF-SOC, the NDC-EKF-SOC still exhibited very accurate SOC estimation — the RMSE for all experimental cases was well within 5%, which meets many standards bodies' guidelines.

Chapter 5

Conclusion

5.1 Summary of Contributions

SOC estimation is of crucial importance for the management of Li-ion batteries to ensure their safety, performance, and life. Based on the recently developed NDC model, this thesis exploits the EKF and UKF to develop new SOC estimation approaches, which are called NDC-EKF-SOC and NDC-UKF-SOC, respectively. Extensive simulations showed that the NDC-EKF-SOC and NDC-UKF-SOC algorithms achieved comparable performance. Both of these algorithms demonstrated accurate SOC tracking while maintaining low computational complexity. Lastly, the NDC-EKF-SOC and NDC-UKF-SOC methodologies were validated through experiments done on a Panasonic lithium-ion cell.

5.2 Future Work

The future is promising for further innovation in the renewable energy industry and, by consequence, the battery industry as well. In particular, future work to be done on the NDC-based SOC estimation algorithms can incorporate adaptive noise estimation, temperature and C-rate awareness, explore machine learning methods, and address the problem of extending the SOC estimation to entire battery modules and packs. First, the SOC estimation can be improved via adaptive noise estimation. The ability to characterize the noise affecting a system, in real-time, would be beneficial for state estimation in real-world systems where the process noise is unknown and typically an educated guess is made regarding its value. Secondly, the NDC model can be extended

to be temperature-aware. The parameters in the model can be made temperature-dependent. This is especially important for the resistance parameters, because the internal resistance and temperature relationship is nonlinear, and the estimation may diverge at high or low temperatures if the resistance parameters do not reflect this relationship. Temperature awareness is an important consideration for real-world systems, as it is desirable for battery systems to work in low temperature environments such as batteries in large vessels in the Atlantic Ocean, or conversely in hot weather conditions such as electric vehicles or grid energy storage in regions with warmer climates. Also, as computing power continues to grow, machine learning algorithms and big data are becoming more practical. As such, a continuation of this work would involve applying machine learning to learn the effects of temperature and C-rate on the model and filter parameters. Finally, another future investigation would be to extend the analysis from a singular cell to a whole battery pack. This is a much more realistic and complex problem — most battery systems consist of multiple cells in series, parallel, or some combination. Understanding the interaction between cells, modules, packs, etc., will be of great importance in the application of these estimation algorithms in an embedded BMS.

References

[1] N. Tian, H. Fang, J. Chen, and Y. Wang. Nonlinear double-capacitor model for rechargeable batteries: modeling, identification, and validation. *IEEE Transactions on Control Systems Technology*, pages 1–15, 2020.

[2] M.A. Hannan, M.S.H. Lipu, A. Hussain, and A. Mohamed. A review of lithium-ion battery state of charge estimation and management system in electric vehicle applications: Challenges and recommendations. *Renewable and Sustainable Energy Reviews*, 78:834 – 854, 2017. ISSN 1364-0321.

[3] Q. Wang, P. Ping, X. Zhao, G. Chu, J. Sun, and C. Chen. Thermal runaway caused fire and explosion of lithium ion battery. *Journal of Power Sources*, 208:210 – 224, 2012. ISSN 0378-7753.

[4] G.L. Plett. *Battery Management Systems, Volume II: Equivalent-Circuit Methods*. Artech House Power Engineering Series. Artech House, 2015. ISBN 9781630810283.

[5] V. Pop, H.J. Bergveld, D. Danilov, P. PL Regtien, and P. HL Notten. State-of-the-art of battery state-of-charge determination. *Battery Management Systems: Accurate State-of-Charge Indication for Battery-Powered Applications*, pages 11–45, 2008.

[6] Y. Wang, H. Fang, L. Zhou, and T. Wada. Revisiting the state-of-charge estimation for lithium-ion batteries: A methodical investigation of the extended kalman filter approach. *IEEE Control Systems Magazine*, 37(4):73–96, Aug 2017.

[7] M. Charkhgard and M. Farrokhi. State-of-charge estimation for lithium-ion batteries using neural networks and EKF. *IEEE Transactions on Industrial Electronics*, 57(12):4178–4187, 2010.

[8] J.N. Hu, J.J. Hu, H.B. Lin, X.P. Li, C.L. Jiang, X.H. Qiu, and W.S. Li. State-of-charge estimation for battery management system using optimized support vector machine for regression. *Journal of Power Sources*, 269:682–693, 2014. ISSN 0378-7753.

[9] S. Dey, B. Ayalew, and P. Pisu. Nonlinear robust observers for state-of-charge estimation of lithium-ion cells based on a reduced electrochemical model. *IEEE Transactions on Control Systems Technology*, 23(5):1935–1942, 2015.

[10] R. Klein, N. A. Chaturvedi, J. Christensen, J. Ahmed, R. Findeisen, and A. Kojic. Electrochemical model based observer design for a lithium-ion battery. *IEEE Transactions on Control Systems Technology*, 21(2):289–301, 2013.

[11] L. Zhang, B. Tiwana, Z. Qian, Z. Wang, R.P. Dick, Z.M. Mao, and L. Yang. Accurate online power estimation and automatic battery behavior based power model generation for smartphones. In *Proceedings of the Eighth IEEE/ACM/IFIP International Conference on Hardware/Software Codesign and System Synthesis*, CODES/ISSS '10, pages 105–114, New York, NY, USA, 2010. ACM. ISBN 978-1-60558-905-3.

[12] G.L. Plett. *Battery Management Systems, Volume I: Battery Modeling*. Artech House Power Engineering Series. Artech House, 2015. ISBN 9781630810245.

[13] I.S. Kim. The novel state of charge estimation method for lithium battery using sliding mode observer. *Journal of Power Sources*, 163(1):584–590, 2006. ISSN 0378-7753. Special issue including selected papers presented at the Second International Conference on Polymer Batteries and Fuel Cells together with regular papers.

[14] Y. Wang, H. Fang, Z. Sahinoglu, T. Wada, and S. Hara. Adaptive estimation of the state of charge for lithium-ion batteries: Nonlinear geometric observer approach. *IEEE Transactions on Control Systems Technology*, 23(3):948–962, 2015.

[15] B.D.O. Anderson and J.B. Moore. *Optimal Filtering*. Dover Books on Electrical Engineering. Dover Publications, 2012. ISBN 9780486136899.

[16] H. Fang, N. Tian, Y. Wang, M. Zhou, and M. A. Haile. Nonlinear Bayesian estimation: from Kalman filtering to a broader horizon. *IEEE/CAA Journal of Automatica Sinica*, 5(2): 401–417, 2018.

[17] Battery University. BU-301a: Types of Battery Cells, 2019. https://batteryuniversity.com/learn/article/types_of_battery_cells.

[18] K. Hagerty. Deep Cycle Batteries Introduction. https://www.altestore.com/howto/deep-cycle-batteries-introduction-a85/, 1999.

[19] J.E.B. Randles. Kinetics of rapid electrode reactions. *Discussions of the faraday society*, 1: 11–19, 1947.

[20] S. Nejad, D.T. Gladwin, and D.A. Stone. A systematic review of lumped-parameter equivalent circuit models for real-time estimation of lithium-ion battery states. *Journal of Power Sources*, 316:183–196, 2016. ISSN 0378-7753.

[21] V.H. Johnson. Battery performance models in ADVISOR. *Journal of Power Sources*, 110(2): 321–329, 2002. ISSN 0378-7753.

[22] V.H. Johnson, A.A. Pesaran, and T. Sack. Temperature-dependent battery models for high-power lithium-ion batteries. In *17th Annual Electric Vehicle Symposium*, Jan. 2001.

[23] H. Fang, Y. Wang, and J. Chen. Health-aware and user-involved battery charging management for electric vehicles: Linear quadratic strategies. *IEEE Transactions on Control Systems Technology*, 25(3):911–923, May 2017.

[24] H. Fang, C. Depcik, and V. Lvovich. Optimal pulse-modulated lithium-ion battery charging: Algorithms and simulation. *Journal of Energy Storage*, 15:359–367, 2018. ISSN 2352-152X.

[25] N. Tian, H. Fang, and J. Chen. A new nonlinear double-capacitor model for rechargeable batteries. In *Proceedings of the 44th Annual Conference of the IEEE Industrial Electronics Society*, pages 1613–1618, 2018.

[26] C.T. Chen. *Linear System Theory and Design*. Oxford University Press, Inc., New York, NY, USA, 3rd edition, 1998. ISBN 0195117778.

[27] M. Proctor, N. Tian, and H. Fang. State-of-charge estimation for batteries based on the non-linear double-capacitor model and extended kalman filter. In *2020 IEEE Green Technologies Conference(GreenTech)*, pages 10–15, 2020.

[28] Z. Chen, Y. Fu, and C. C. Mi. State of charge estimation of lithium-ion batteries in electric drive vehicles using extended Kalman filtering. *IEEE Transactions on Vehicular Technology*, 62(3):1020–1030, March 2013.

[29] W. Junping, G. Jingang, and D. Lei. An adaptive Kalman filtering based State of Charge combined estimator for electric vehicle battery pack. *Energy Conversion and Management*, 50(12):3182 – 3186, 2009. ISSN 0196-8904.

[30] H. Fang, Y. Wang, Z. Sahinoglu, T. Wada, and S. Hara. Adaptive estimation of state of charge for lithium-ion batteries. In *2013 American Control Conference*, pages 3485–3491, June 2013.

[31] H. Fang, Y. Wang, Z. Sahinoglu, T. Wada, and S. Hara. State of charge estimation for lithium-ion batteries: An adaptive approach. *Control Engineering Practice*, 25:45 – 54, 2014.

[32] J. Han, D. Kim, and M. Sunwoo. State-of-charge estimation of lead-acid batteries using an adaptive extended Kalman filter. *Journal of Power Sources*, 188(2):606–612, 2009. ISSN 0378-7753.

[33] A. Vasebi, S.M.T. Bathaee, and M. Partovibakhsh. Predicting state of charge of lead-acid batteries for hybrid electric vehicles by extended Kalman filter. *Energy Conversion and Management*, 49(1):75 – 82, 2008. ISSN 0196-8904.

[34] EPA. The EPA Urban Dynamometer Driving Schedule (UDDS), 2017. https://www.epa.gov/sites/production/files/2015-10/uddscol.txt.

[35] E. A. Wan and R. Van Der Merwe. The unscented kalman filter for nonlinear estimation. In *Proceedings of the IEEE 2000 Adaptive Systems for Signal Processing, Communications, and Control Symposium (Cat. No.00EX373)*, pages 153–158, Oct 2000.

[36] K. S. Ng, C.S. Moo, Y.P. Chen, and Y.C. Hsieh. Enhanced coulomb counting method for estimating state-of-charge and state-of-health of lithium-ion batteries. *Applied Energy*, 86 (9):1506–1511, 2009. ISSN 0306-2619.